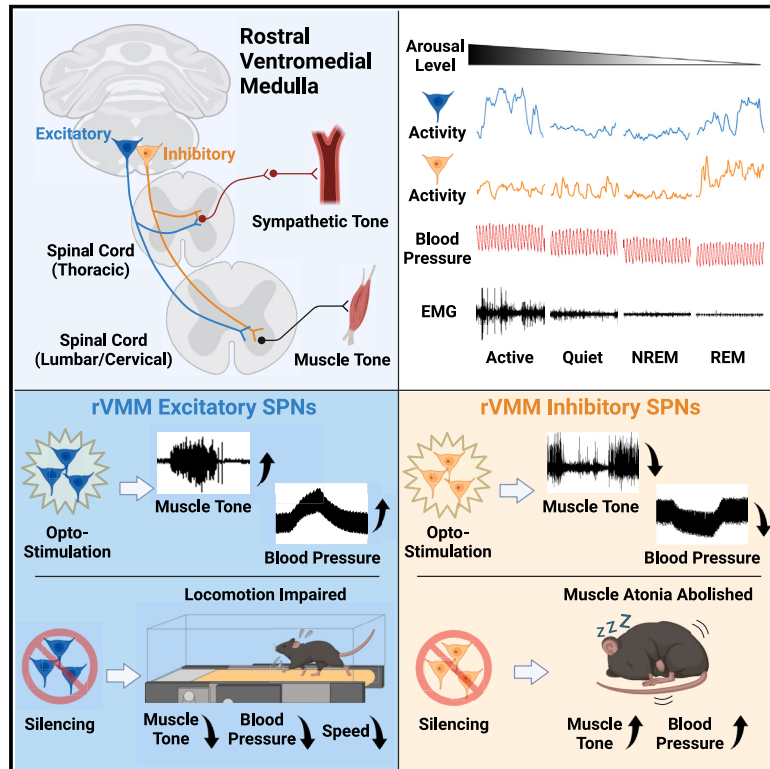# Spinal projecting neurons in rostral ventromedial medulla co-regulate motor and sympathetic tone

Graphical abstract

Authors

Zicong Zhang, Junfeng Su, Jing Tang, ..., Chinfei Chen, Michael J. Prerau, Zhigang He

Correspondence

zhigang.he@childrens.harvard.edu

In brief

The spinal projecting neurons in the rostral ventromedial medulla co-innervate sympathetic preganglionic neurons and motor-related regions in the spinal cord. The excitatory and inhibitory populations in this same brainstem region have opposite functions in regulating somatic and sympathetic tone in different arousal states.

Highlights

- SPNs in rVMM co-innervate sympathetic and motor regions in the spinal cord

- Excitatory and inhibitory rVMM SPNs control motor and sympathetic function oppositely

- Excitatory rVMM SPNs set motor and sympathetic tone for locomotion performance

- Inhibitory rVMM SPNs regulate muscle atonia and sympathetic hypoactivity in REM sleep

Cell

Article

Spinal projecting neurons in rostral ventromedial medulla co-regulate motor and sympathetic tone

Zicong Zhang,[1,2,12] Junfeng Su,[1,2,12] Jing Tang,[1,2] Leeyup Chung,[1,2] Jessica C. Page,[1,2] Carla C. Winter,[1,2,3] Yuchu Liu,[1,2] Evgenii Kegeles,[1,2,4] Sara Conti,[1,2] Yu Zhang,[1,2] Jason Biundo,[1,2] Joshua I. Chalif,[1,5] Charles Y. Hua,[1,2] Zhiyun Yang,[1,2] Xue Yao,[1,2] Yang Yang,[1,2] Shuqiang Chen,[6] Jan M. Schwab,[7,8] Kuan Hong Wang,[9] Chinfei Chen,[1,2] Michael J. Prerau,[10,11] and Zhigang He[1,2,13,*]

[1]F.M. Kirby Neurobiology Center, Boston Children's Hospital, Boston, MA, USA
[2]Department of Neurology and Ophthalmology, Harvard Medical School, Boston, MA, USA
[3]Harvard/MIT MD-PhD Program, Harvard Medical School, Boston, MA, USA
[4]PhD Program in Biological and Biomedical Sciences, Harvard Medical School, Boston, MA, USA
[5]Department of Neurosurgery, Brigham and Women's Hospital, Boston, MA, USA
[6]Graduate Program for Neuroscience, Boston University, Boston, MA, USA
[7]Belford Center for Spinal Cord Injury, The Ohio State University, Columbus, OH, USA
[8]Departments of Neurology and Neuroscience, College of Medicine, The Ohio State University, Columbus, OH, USA
[9]Department of Neuroscience, University of Rochester Medical Center, Rochester, NY, USA
[10]Division of Sleep and Circadian Disorders, Brigham and Women's Hospital, Boston, MA, USA
[11]Department of Medicine, Harvard Medical School, Boston, MA, USA
[12]These authors contributed equally
[13]Lead contact
*Correspondence: zhigang.he@childrens.harvard.edu
https://doi.org/10.1016/j.cell.2024.04.022

SUMMARY

Many behaviors require the coordinated actions of somatic and autonomic functions. However, the underlying mechanisms remain elusive. By opto-stimulating different populations of descending spinal projecting neurons (SPNs) in anesthetized mice, we show that stimulation of excitatory SPNs in the rostral ventromedial medulla (rVMM) resulted in a simultaneous increase in somatomotor and sympathetic activities. Conversely, opto-stimulation of rVMM inhibitory SPNs decreased both activities. Anatomically, these SPNs innervate both sympathetic preganglionic neurons and motor-related regions in the spinal cord. Fiber-photometry recording indicated that the activities of rVMM SPNs correlate with different levels of muscle and sympathetic tone during distinct arousal states. Inhibiting rVMM excitatory SPNs reduced basal muscle and sympathetic tone, impairing locomotion initiation and high-speed performance. In contrast, silencing the inhibitory population abolished muscle atonia and sympathetic hypoactivity during rapid eye movement (REM) sleep. Together, these results identify rVMM SPNs as descending spinal projecting pathways controlling the tone of both the somatomotor and sympathetic systems.

INTRODUCTION

Numerous human and animal behaviors involve the coordinated engagement of somatomotor and autonomic systems. For example, running and flight-or-fight responses require elevated skeletal motor activities with concurrent increases in respiration, heart rate, and blood pressure.[1,2] Conversely, during rapid eye movement (REM) sleep, muscle atonia often accompanies reduced sympathetic activities.[3,4] These observations imply the presence of neural circuits that can simultaneously control the activities of both the somatomotor and autonomic systems. Motor and pre-motor neurons reside in all spinal segments and control hundreds of muscles in the body. Likewise, sympathetic preganglionic neurons (SPGNs) reside in the T1 to L2 spinal seg-

ments, regulating blood pressure and other sympathetic functions.[5] However, ample evidence suggests that brain-derived supraspinal inputs are critical for coordinating somatomotor and sympathetic functions.[6–9] For example, patients and animal models of spinal cord injury exhibit paralysis and autonomic dysfunction.[10–12] Attempted muscle contraction in paralyzed human subjects increased blood pressure and heart rates.[13–15]

In mammals, brain commands are mainly carried to the spinal cord by different populations of descending spinal projecting neurons (SPNs).[16–19] Thus, a key challenge is to define how these SPNs execute and coordinate such diverse command functions via their long axonal projections. Tremendous progress has been made in analyzing the effects of individual brain regions and their respective spinal projections on motor, sensory,
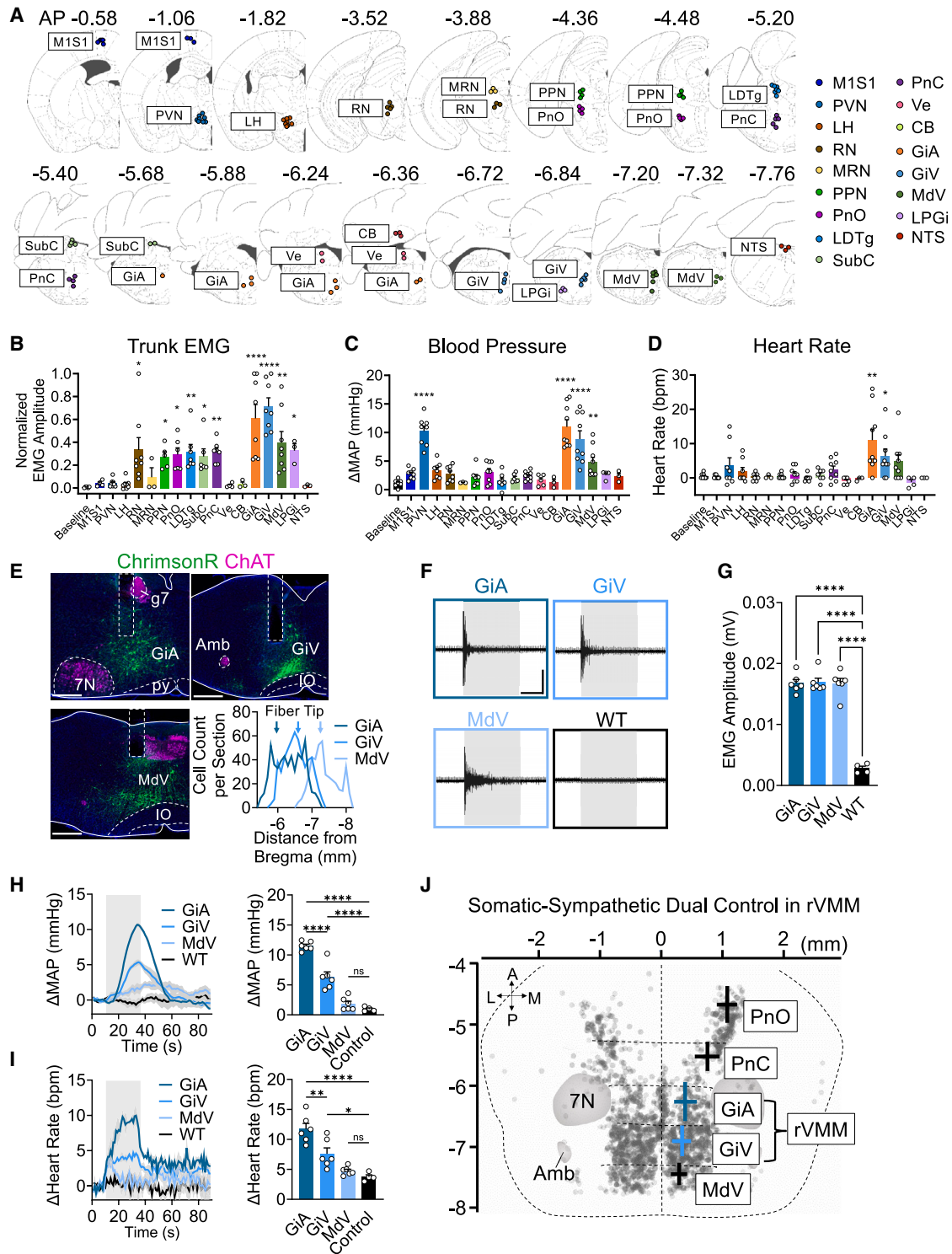
Figure 1. Opto-stimulation mapping of excitatory SPNs controlling somatomotor and/or sympathetic responses in anesthetized mice

(A) Coordinates of fiber-optic tips targeting different populations of *Vglut2*^{+} SPNs.

(B–D) Average (±SEM) changes of EMG responses (normalized to the maximum amplitude within same subject) (B), mean arterial pressure (MAP) (C), or heart rate (D, with the presence of muscle relaxant), upon stimulating different populations of *Vglut2*^{+} SPNs, *, $p < 0.05$; **, $p < 0.01$; ****, $p < 0.0001$; Kruskal-Wallis test with Dunn's multiple comparisons.

(legend continued on next page)

and sympathetic functions.[17,18,20–28] By contrast, much less is known about the mechanisms underlying their coordination. It remains unknown whether or which populations of SPNs directly control both sympathetic (SPGNs) and motor (spinal motor and pre-motor) neurons and mediate their functional coordination. To address these questions, we optimized an adeno-associated virus (AAV)-based method to target brain-wide SPNs efficiently and surveyed their functions in anesthetized mice. These results revealed that the SPNs in the rostral ventromedial medulla (rVMM) can co-regulate somatic muscles and sympathetic activities, with the excitatory and inhibitory populations in this same region exhibiting the opposite outcomes. Further studies suggested that these specific groups of SPNs complementarily control the tone of skeletal muscles and sympathetic activities in different arousal states, thereby governing state-dependent behavioral performance.

RESULTS

An optimized procedure for efficient labeling of SPNs

SPNs are sparsely distributed in different brain regions, and their axonal projections frequently overlap in the spinal cord. To target them selectively and efficiently, we developed a retrograde labeling procedure with a new version of the highly diffusible AAV vector and an intraspinal injection protocol targeting the entire spinal cord. In light of the superior diffusion capacity of AAV9,[29] we inserted the 10-mer peptide, which is critical for the retrograde targeting capability of AAV2retro,[30] into the AAV9 capsid, generating a retrograde competent AAV9 vector, named AAV9retro. Then, we optimized a multiple injection protocol to cover the cervical, thoracic, and lumbar spinal cord (C3-L6) of mice at postnatal day 14 (P14) when the spinal cord is still relatively small in size, yet its development is largely completed (Figure S1A).[31,32] This protocol labeled brain-wide SPNs in the cortex, hypothalamus, midbrain, cerebellum, pons, and medulla (Figure S1B). With another tracer red retrobeads as a reference, we estimated 90% SPNs in the cortex and midbrain, and 70% SPNs in the hypothalamus and brainstem were labeled by AAV9-retro (Figure S1C). In addition to excitatory and inhibitory SPNs (Figure S1D), our method also labels tyrosine hydroxylase positive (TH[+]) SPNs in the pons and serotonergic positive (5-HT[+]) SPNs in para-pyramidal area of the medulla; however, few TH[+] SPNs or 5-HT[+] SPNs were observed in the medulla areas or caudal raphe, respectively (Figures S1E–S1G), perhaps due to the tropism biases of AAV9retro vectors against certain types of modulatory neurons.[33,34]

Opto-stimulation-assisted mapping of excitatory SPNs controlling sympathetic and/or somatomotor responses

We next applied optogenetic stimulation to the labeled SPNs to map their effects on motor (electromyography [EMG] of the trunk muscle longissimus thoracis) and sympathetic (blood pressure and heart rate) activities in anesthetized mice. Because excitatory and inhibitory SPNs spatially overlap in some brain regions (Figure S1D), a non-selective stimulation may not reveal their specific functions. Thus, we analyzed the excitatory SPNs by injecting AAV9retro-expressing Cre-dependent channelrhodopsin (AAV9retro-DIO-ReaChR-citrine) to the spinal cord of P14 Vglut2-Cre mice (Figure S1H).[35] A low-intensity laser, which evoked a blood pressure response only within 0.5 mm from the fiber-optic tip (Figure S1J), was selected for further mapping.

With these optimizations, we stimulated the Vglut2^{+} SPNs in 17 brain regions (Figure 1A) and recorded trunk muscle EMG in anesthetized mice (Figure 1B). Because muscle activity can modulate blood pressure independent of descending control, we then recorded blood pressure and heart rate in the presence of the muscle relaxant pancuronium (Figure 1C).[36,37] No significant responses in EMG, blood pressure, or heart rate occurred after stimulation of several regions, including primary motor/somatosensory cortices (M1/S1), lateral hypothalamus (LH), mesencephalic reticular nucleus (MRN), vestibular nucleus (Ve), fastigial and interposed deep cerebellar nuclei (CB), and solitary nucleus (NTS), possibly due to the low stimulation intensity and/or limited numbers of labeled SPNs. However, we identified three types of responses in other regions. First, stimulation of SPNs in seven regions, including red nucleus (RN), pedunculopontine nucleus (PPN), pontine reticular nucleus oral part (PnO), laterodorsal tegmental nucleus (LDTg), subcoeruleus nucleus (SubC), pontine reticular nucleus caudal part (PnC), and lateral paragigantocellular nucleus (LPGi), elicited predominantly EMG responses (Figures 1B–1D). Second, stimulation of SPNs in the paraventricular nucleus (PVN) of the hypothalamus only increased blood pressure but did not impact trunk EMG response (Figures 1B–1D), consistent with previous findings of spinal projections from PVN.[38] Third, stimulation of the SPNs at different rostral-caudal levels of the ventromedial medulla, equivalent to gigantocellular reticular nucleus alpha part (GiA), ventral part (GiV), and medullary reticular nucleus (MdV), elicited consistent EMG responses, as well as robust blood pressure and ;heart rate increases in the presence of pancuronium (Figures 1B–1D).

In the experiments described above, ReaChR-citrine protein is present in both SPN cell bodies and processes. Thus, the observed responses could result from stimulating labeled SPNs in situ and/or the passing fibers of other SPNs. To address this,

(E) Representative images showing fiber-optic tip (white rectangles) and soma locations of the intersectionally labeled Vglut2^{+} SPNs in GiA, GiV, and MdV, respectively. Bottom right: cell distribution and fiber-optic tip location along rostral-caudal axis. Scale bars, 200 μm. 7N, facial nucleus; g7, genu of the facial nerve; py, pyramidal tract; Amb, ambiguus nucleus; IO, inferior olive.

(F) Representative EMG responses upon opto-stimulation (gray shade) in GiA, GiV, or MdV with ChrimsonR-expressing SPNs or in GiA of control in control wild-type mice received the same virus injection. EMG scale bars, 0.01 mV; timescale bars, 10 s.

(G) Average (±SEM) maximal EMG responses upon opto-stimulation. ****, $p < 0.0001$, one-way ANOVA with Dunnett's multiple comparison test.

(H and I) Time course (left) and maximum changes (right, average ± SEM) of MAP (H) and heart rate (I) upon stimulation (gray shade) from baseline (10 s before stimulation). *, $p < 0.05$; **, $p < 0.01$; ****, $p < 0.0001$, ns, not significant; one-way ANOVA with Tukey's multiple comparison test.

(J) Stimulation sites with somatomotor and sympathetic responses.

See also Figure S1.
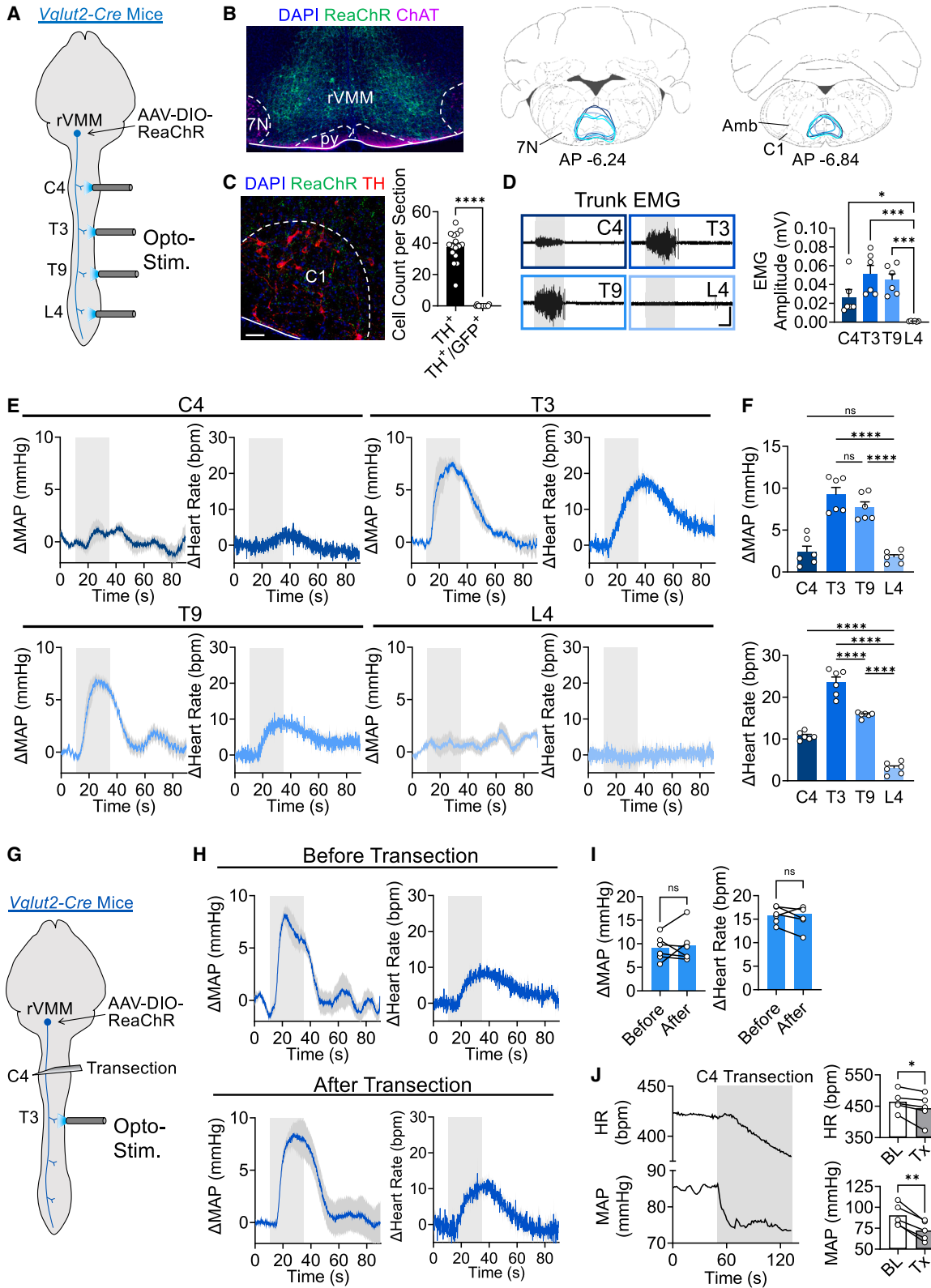
(legend on next page)

we used an intersectional strategy to selectively express a different version of channelrhodopsin, ChrimsonR, in the excitatory SPNs at different levels of the ventromedial medulla (Figure S1K). Optical fibers were positioned at the center of each site, and their locations were verified with post hoc histology (Figures 1E and S1L). Without the muscle relaxant, stimulation of SPNs in all sites induced robust EMG responses (Figures 1F and 1G). With the presence of pancuronium, stimulation of GiA induced the most robust increase of blood pressure and heart rate, while stimulation of GiV induced smaller responses. Post hoc histology showed that the number of neurons labeled in GiA and GiV was similar (Figure S1K). Stimulating the SPNs in MdV induced no increase in blood pressure or heart rate (Figures 1H and 1I). Thus, the excitatory SPNs in the rVMM, covering both GiA and GiV, have a dual function in activating both sympathetic and somatomotor functions (Figure 1J).

Excitatory rVMM SPNs co-control somatomotor and sympathetic function via their direct spinal projections

Although several brain regions may regulate cardiovascular functions,[20,39,40] current studies have been primarily focused on the rostral ventrolateral medulla (rVLM).[20] In this region, a subset of C1 adrenergic neurons send their projections to the spinal cord and impact blood pressure and other sympathetic functions.[21,22] However, the rVMM SPNs differ from C1 neurons. First, besides having different soma locations, these neurons have distinct terminations in the spinal cord. rVMM SPNs innervate the spinal areas related to motor and sympathetic control (see below). By contrast, the spinal projections of C1 neurons, labeled by stereotaxic injection of AAV8-DIO-ReaChR-citrine in the rVLM of *TH-Cre* mice (Figures S2A and S2B),[41] terminate nearly exclusively in the intermediolateral column (IML) where the SPGNs are located (Figures S2C and S2D). Second, opto-stimulation of these TH^+ neurons (including C1 neurons) in the rVLM increased blood pressure but elicited no EMG response in the trunk muscles (Figures S2E and S2F). Consistently, pancuronium had little effect on the extent of the stimulation-induced increase in blood pressure (Figure S2F). In addition, as mentioned above, our retrograde labeling protocol labeled very few TH^+ cells in the medulla.

We next considered the possibility that the rVMM excitatory SPNs send projections to the rVLM and indirectly impact sympa-

thetic functions. We thus examined the impact of opto-stimulation on the spinal projections of rVMM excitatory SPNs. We injected AAV8-DIO-ReaChR-citrine into the rVMM of adult *Vglut2-Cre* mice and performed opto-stimulation at different spinal levels (Figures 2A and 2B). We found that opto-stimulation at the thoracic level (T3 or T9) induced trunk EMG response (Figure 2D) and increased blood pressure and heart rate (Figures 2E and 2F). Importantly, this effect remained even after spinal cord transection at the cervical level (Figures 2G–2I), although the basal blood pressure and heart rate levels were reduced after spinal transection (Figure 2J).[42] Post hoc histology verified that nearly no TH^+ cells in rVLM were labeled by virus diffusion (2 out of 603 TH^+ cells were co-labeled with ReaChR; Figure 2C). Together, excitatory rVMM SPNs control sympathetic response through their spinal projections.

Inhibitory rVMM SPNs are also dual functioning but in an opposing manner to the excitatory population

We next examined the effect of opto-stimulation of inhibitory SPNs in rVMM on blood pressure, heart rate, and motor responses. We expressed ReaChR in these neurons by injecting AAV9retro viruses expressing FlpO-dependent Cre (AAV9retro-fDIO-Cre) to the entire spinal cord at P14 and Cre-dependent ReaChR AAVs (AAV-DIO-ReaChR) to rVMM of *Vgat-FlpO* mice, which label both GABAergic and glycinergic inhibitory SPNs (Figures 3A and S2G).[43] Because anesthetics inhibit motor activity, we performed the experiments at two different levels of anesthesia. First, in a deeply anesthetized condition where EMG activities are absent, stimulating rVMM inhibitory SPNs reduced blood pressure and heart rate at a modest amplitude (Figures 3D and 3E). Second, to examine the inhibitory effect on EMGs, we allowed mice to slightly recover from anesthesia to a level where small but constant basal-level EMGs were observed (Figure 3B, middle and lower panels). Stimulating rVMM inhibitory SPNs suppressed EMG activities (Figures 3B and 3C) and blood pressure (Figures 3F and 3G). The larger reduction in the lightly anesthetized condition might be due to the higher basal blood pressure level than deep anesthesia (Figure 3H). Post hoc histology of c-Fos expression confirmed that most rVMM SPNs labeled with ReaChR were activated with opto-stimulation through the optical fiber implanted in the rVMM at the same intensity as applied in the above experiment (Figures S2H and S2I). In addition, stimulating

---

Figure 2. Excitatory rVMM SPNs control somatomotor and sympathetic functions through spinal projections in anesthetized mice

(A) Experimental scheme.

(B) Left: image of brainstem coronal section showing the expression of ReaChR in rVMM. Right: ReaChR expression areas in two coronal levels of rVMM, colors marked for different subjects, n = 6.

(C) Immunostaining image (left) and cell counts (right) showing nearly no ReaChR expression diffused to C1 neurons. Quantification from 16 sections of 6 mice. ****, $p < 0.0001$; unpaired t test.

(D) Examples and average (±SEM) maximal EMG responses upon opto-stimulation (gray shade) at different spinal cord levels. EMG scale bars, 0.05 mV; timescale bars, 10 s. *, $p < 0.05$; ***, $p < 0.001$; one-way ANOVA with Dunnett's multiple comparison test.

(E and F) Time course (E) and maximal changes (F, mean ± SEM) of MAP and heart rate upon opto-stimulation (gray shade) at different spinal cord levels. ****, $p < 0.0001$; ns, not significant; one-way ANOVA with Tukey's multiple comparison test.

(G) Scheme of assessing the effects of local stimulation of ReaChR-expressing axons from excitatory SPNs in rVMM after C4 spinal transection.

(H and I) Time course (H) and maximal changes (I, mean ± SEM) of MAP and heart rate upon opto-stimulation (gray shade) at T3 before and after cervical transection. ns, not significant; paired t test.

(J) Representative trace (left panel) and average change of blood pressure and heart rate after C4 transection. *, $p < 0.05$; **, $p < 0.01$; paired t test. BL, baseline; Tx, transection.
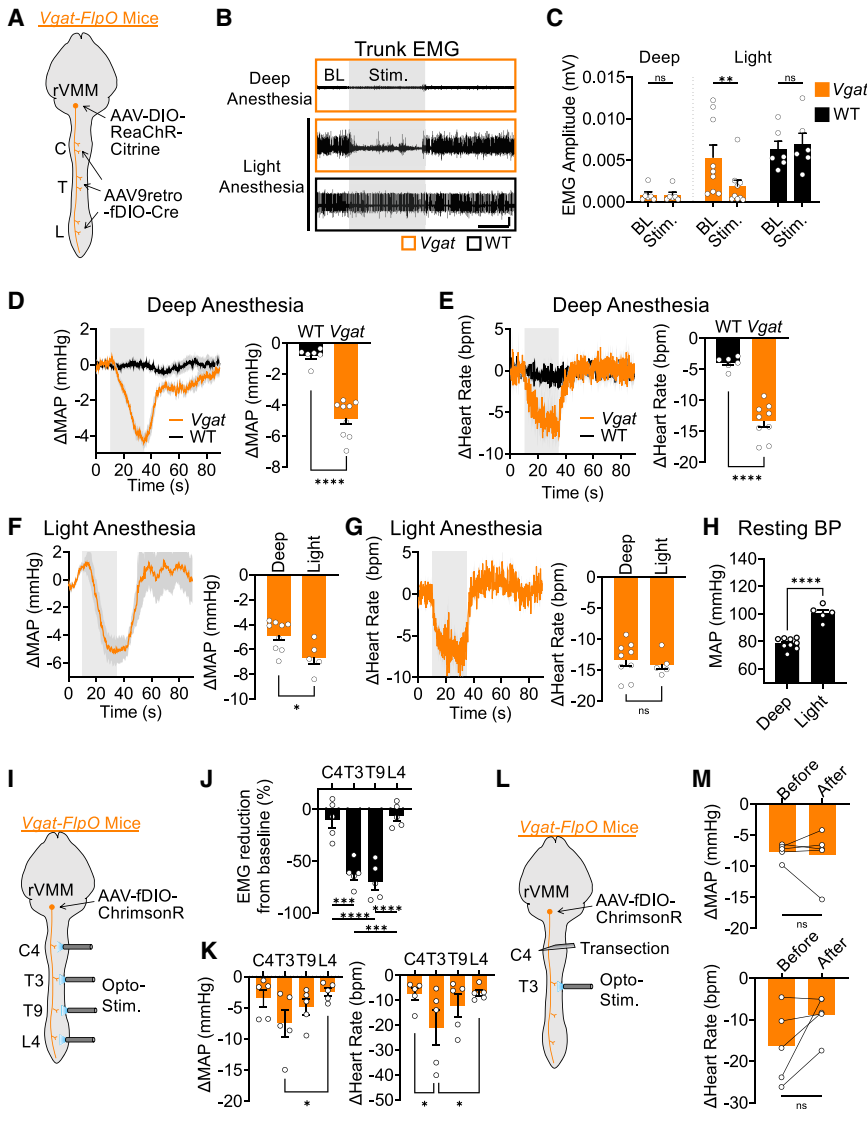
See also Figure S2.

Figure 3. Inhibitory rVMM SPNs suppress somatomotor and sympathetic activities in anesthetized mice

(A) Experimental scheme.

(B) Examples of EMG responses upon opto-stimulation (gray shade) under deep or light anesthesia in *Vgat-FlpO* mice (orange outline) or WT mice (black outline). EMG scale bars, 0.01 mV. Time-scale bars, 10 s. BL: baseline.

(C) Average (±SEM) EMG amplitude during baseline (BL) and opto-stimulation (Stim.) in deep or light anesthesia conditions in *Vgat-FlpO* mice (orange) or WT mice (black). **, $p < 0.01$; ns, not significant; two-way ANOVA with Bonferroni's multiple comparisons test.

(D and E) Time course (left) and maximal changes (right, average ± SEM) of MAP and heart rate upon opto-stimulation in deep anesthesia with muscle relaxant. ****, $p < 0.0001$; unpaired t test.

(F and G) Time course (left) and maximal changes (right, average ± SEM) of MAP and heart rate upon opto-stimulation in lightly anesthetized condition, compared with deep anesthesia. *, $p < 0.05$; ns, not significant; unpaired t test.

(H) Comparison of resting blood pressure between deep and light anesthesia. ****, $p < 0.0001$; unpaired t test.

(I) Experimental scheme to express ChrimsonR in the inhibitory SPNs in rVMM and stimulate their spinal cord projections at different spinal levels.

(J) Average (±SEM) EMG reduction upon opto-stimulation at different spinal cord levels. ***, $p < 0.001$; ****, $p < 0.0001$; one-way ANOVA with Tukey's multiple comparison test.

(K) Maximal reduction (mean ± SEM) of MAP and heart rate upon opto-stimulation at different spinal cord levels. *, $p < 0.05$; one-way ANOVA with Fisher's LSD test.

(L) Scheme of assessing the effects of stimulating the spinal projections of inhibitory SPNs in rVMM after C4 spinal transection.

(M) Maximal reduction (mean ± SEM) of MAP and heart rate upon opto-stimulation at T3 before and after cervical transection. ns, not significant; paired t test.

---

the ReaChR-expressing spinal projections of the rVMM inhibitory SPNs at the thoracic spinal cord suppressed EMG activities and reduced blood pressure and heart rate both before (Figures 3I–3K) and after cervical spinal cord transection (Figures 3L and 3M), suggesting that the spinal projections directly mediate the inhibitory effect. Taken together, excitatory and inhibitory SPNs in the same rVMM region have the capacity for dual control of sympathetic and somatomotor functions in the spinal cord, but in an opposite direction. This might explain why rVMM has been overlooked in previous studies on sympathetic control.

Spinal and brain projection patterns of excitatory and inhibitory rVMM SPNs

We next used the intersectional labeling strategy to express green fluorescent protein (GFP) and synaptophysin-red-fluorescent-protein (RFP) or syp-RFP in excitatory or inhibitory rVMM SPNs and examined their axon projection (GFP) and presynaptic termi-

nals (syp-RFP) (Figures 4A and 4E). In the spinal cord, both excitatory and inhibitory axons are distributed in the IML (Figures 4B, 4F, S3A, and S3B). Additionally, RFP+ synaptic boutons are colocalized with GFP on the soma and dendrites of the SPGNs stained with anti-ChAT antibodies in the IML of the thoracic cord (Figures 4C and 4G). However, excitatory and inhibitory SPNs exhibited different termination patterns in other spinal areas. Excitatory projections mainly terminate in the intermediate laminae, where pre-motor neurons are concentrated (Figures 4D and S3A).[44] By contrast, inhibitory fibers are enriched in the ventral horn, the location of the spinal motor neurons (Figures 4H and S3B), consistent with previous results of anterograde tracing from similar medulla regions.[45] Intriguingly, many inhibitory, but not excitatory, terminals were observed in the superficial dorsal horn (Figure 4H), suggesting a possibly additional role for the inhibitory population in sensory processing. Thus, both excitatory and inhibitory rVMM SPNs innervate SPGNs for sympathetic

Intersectionally labeled excitatory or inhibitory SPNs in rVMM from the entire spinal cord
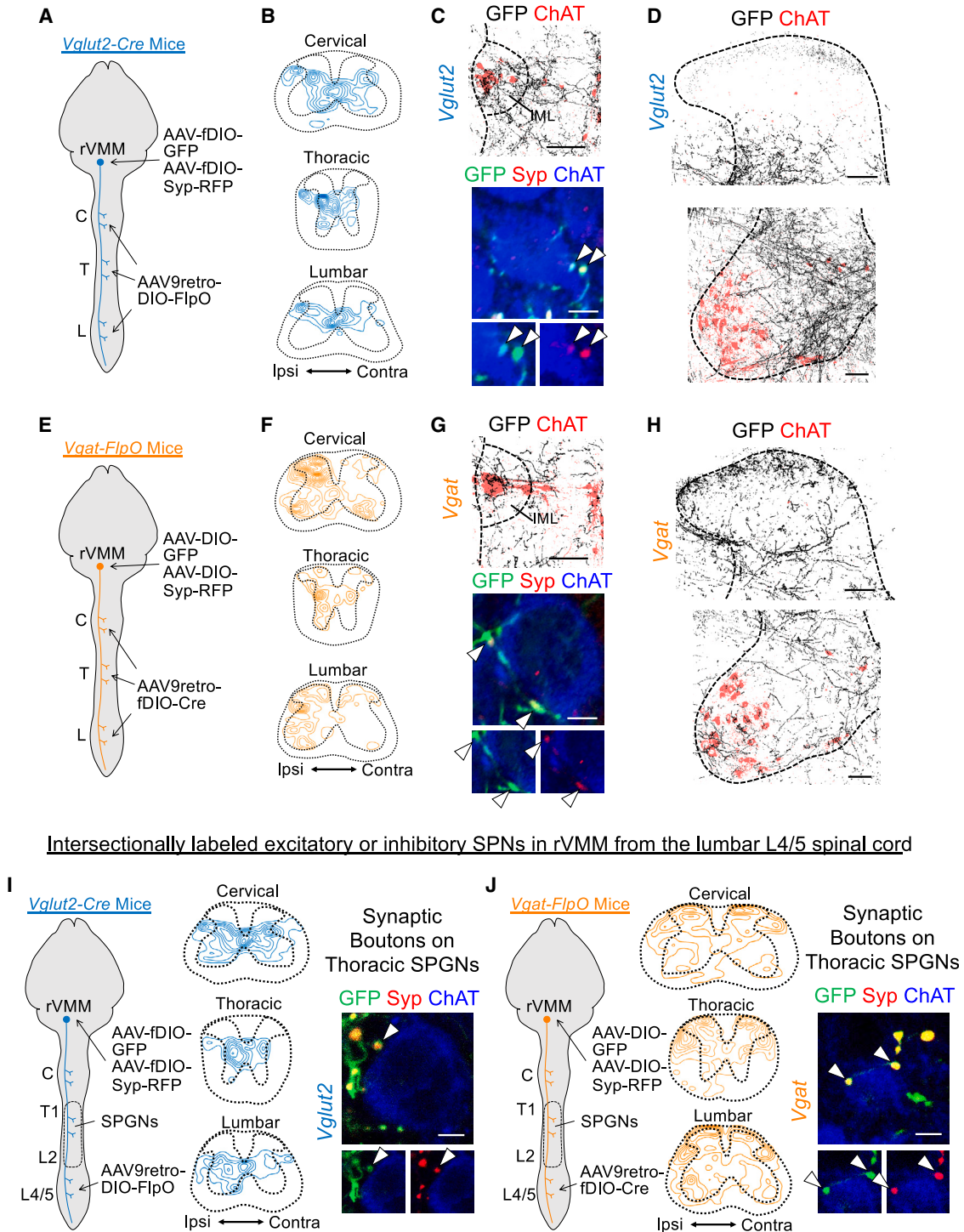
Intersectionally labeled excitatory or inhibitory SPNs in rVMM from the lumbar L4/5 spinal cord

Figure 4. Spinal innervation patterns of excitatory and inhibitory rVMM SPNs

(A) Experimental scheme.

(B) Contour maps of excitatory fiber densities in different spinal levels.

(C) Upper: representative image of excitatory projections in thoracic IML. Scale bars, 100 μm. Lower: excitatory synaptic boutons (labeled by RFP, Syp) colocalize with ChAT$^+$ IML neurons (pointed by white arrow). Scale bars, 5 μm.

(D) Excitatory projections in cervical spinal cord. Scale bars, 100 μm.

(legend continued on next page)

control, while they may regulate somatomotor (or sensory) functions via different circuitries.

In addition, the rVMM SPNs send collateral branches to innervate several nuclei in the medulla, pons, and midbrain (Figure S3). Excitatory and inhibitory SPNs have shared targets, particularly the LDTg and PPN, where cholinergic ascending neurons are located (Figures S3C and S3D). However, these neurons have distinct termination patterns in other regions. For example, excitatory SPNs mainly innervate motor-related cranial nuclei, including facial nucleus (7N), oculomotor nucleus (3N), trochlear nucleus (4N), PnO, and MdV (Figure S3E). However, inhibitory SPN branches were found to be more abundant in broader brain regions related to autonomic and sensory functions, including the NTS, locus coeruleus (LC), SubC ventral part (SubCV), principal sensory trigeminal nucleus (Pr5), A5 and A7 noradrenergic groups, periaqueductal gray (PAG), parabrachial nucleus (PBN), and spinal trigeminal nucleus (Sp5) (Figures S3F and S3G). Noticeably, inhibitory SPNs avoid innervating cranial nerve nuclei 3N and 4N, where the motor neurons controlling eye movements are located (Figure S3H). Thus, the excitatory rVMM SPNs may be relevant in driving motor nuclei, while the inhibitory SPNs may be more important for tuning sensory and autonomic integration.

Previous studies suggest that rVMM SPNs exhibit extensive collaterals in multiple spinal levels.[46–50] We next assessed if the same group of SPNs innervate both motor and sympathetic regions in the spinal cord. Since SPGNs are distributed between T1 to L2,[5] the L4/5 levels are expected to have the neurons for direct somatomotor but not sympathetic control. Therefore, we intersectionally labeled excitatory or inhibitory rVMM SPNs from L4/5 segments and examined their terminations in the spinal cord. We injected a small volume of AAV9retro-DIO-FlpO or AAV9retro-fDIO-Cre to L4/5 of adult *Vglut2-Cre* or *Vgat-FlpO* mice, respectively, followed by AAV-fDIO or DIO-GFP-syp-RFP injection in rVMM (Figures 4I and 4J). To monitor the diffusion of injected viruses in the spinal cord, aliquots of AAV9-H2B-tdTomato were co-injected to L4/5. This procedure resulted in efficient labeling of SPNs in rVMM (Figure S3L) but did not transduce cells in the spinal segments with SPGNs (Figure S3I). Importantly, these L4/5-projecting excitatory and inhibitory SPNs send collateral branches to the thoracic spinal cord (Figures 4I, 4J, S3J, and S3K) and innervate ChAT⁺ SPGNs (Figures 4I and 4J). These results suggest that at least some rVMM SPNs innervate both motor and sympathetic spinal neurons.

Direct synaptic connections between rVMM SPNs and SPGNs

To directly assess synaptic connections between the axons of SPNs and SPGNs, we performed whole-cell patch recording in *ex vivo* slices prepared from the thoracic spinal cord of *ChAT-Cre:tdTomato* reporter mice (to label SPGNs in the IML of the thoracic spinal cord) (Figure S4A). To facilitate opto-stimulation of both excitatory and inhibitory SPN axons, we injected AAV8-ChR2-EYFP into the rVMM of these mice at P4 (Figures S4F–S4H). In horizontal sections of the thoracic spinal cord from mice injected with the virus, we performed whole-cell voltage clamp recordings on *tdTomato⁺* cells in IML while applying LED stimulation on rVMM SPN axon terminals to examine mono- and poly-synaptic excitatory postsynaptic currents (EPSCs) and inhibitory postsynaptic currents (IPSCs). At −70 mV holding potential, optical stimulation produced current responses in 13 of 23 neurons recorded. Post hoc histology verified that most ChR2-EYFP expressions were in the rVMM and none in the C1 region (Figures S4F–S4H). To determine the mono-synaptic component of the evoked response, Tetrodotoxin (TTX) (0.5 μM), 4-Aminopyridine (4-AP) (200 μM), NBQX (5 μM), and CPP (10 μM) were sequentially applied. The sodium channel blocker TTX blocked the EPSC, indicating that the evoked EPSC is action potential dependent. With the addition of the potassium channel blocker 4-AP, which augmented light-induced, direct depolarization of ChR2⁺ axon terminals, EPSCs reappeared. Ionotropic glutamate receptor antagonists (NBQX and CPP) significantly attenuated this EPSC amplitude, demonstrating that rVMM SPNs make mono-synaptic glutamatergic connections onto IML neurons (Figures S4B and S4C).

Notably, outward currents were observed in 9 of the 13 cells in the presence of TTX/4-AP/NBQX/CPP (Figure S4C), suggesting that these cells might also receive inhibitory inputs from the rVMM. We then tested if the observed mono-synaptic outward currents were IPSCs mediated by GABA$_A$ and/or glycine receptors. Holding the membrane potential at +20 mV, mono-synaptic IPSCs were present in 10 of 11 recorded cells. GABA$_A$ and glycine receptor antagonists, BMI (10 μM) and strychnine (1 μM), significantly inhibited the mono-synaptic outward current amplitude to 2.2% of baseline (Figures S4D and S4E). Thus, these results suggest excitatory and inhibitory rVMM SPNs make direct synaptic connections onto SPGNs, although indirect connections may also be present.

Distinct activity patterns of excitatory and inhibitory rVMM SPNs in different arousal states and high-speed locomotion

To explore the behavioral relevance of these rVMM SPNs in behaving mice, we targeted GCaMP6s expression to excitatory or inhibitory rVMM populations (Figure 5A). With an implanted optical fiber (Figure 5B), we recorded their population neuronal activity[51] (Figure 5C) when mice were in two different conditions: (1) in a

(E) Scheme of intersectional labeling of inhibitory SPNs in rVMM with GFP and synapse-targeting RFP.

(F) Contour maps of inhibitory fiber densities in different levels of the spinal cord.

(G) Upper: representative image of inhibitory projections in thoracic IML. Scale bars, 100 μm. Lower: excitatory synaptic boutons (labeled by RFP, Syp) colocalize with ChAT⁺ IML neurons (pointed by white arrow). Green and red channels of the pointed structure are split below. Scale bars, 5 μm.

(H) Inhibitory projections in cervical spinal cord. Scale bars, 100 μm.

(I and J) Left: scheme of intersectional labeling of L4/5-projecting excitatory (I) or inhibitory (J) rVMM SPNs with GFP and synapse-targeting RFP. Middle: contour maps of excitatory fiber densities at different spinal levels, derived from lumbar projecting SPNs. Right: excitatory synaptic boutons (Syp, RFP), derived from lumbar projecting SPNs, terminated on ChAT⁺ IML neurons in thoracic spinal cord (pointed by white arrow). Scale bars, 5 μm.
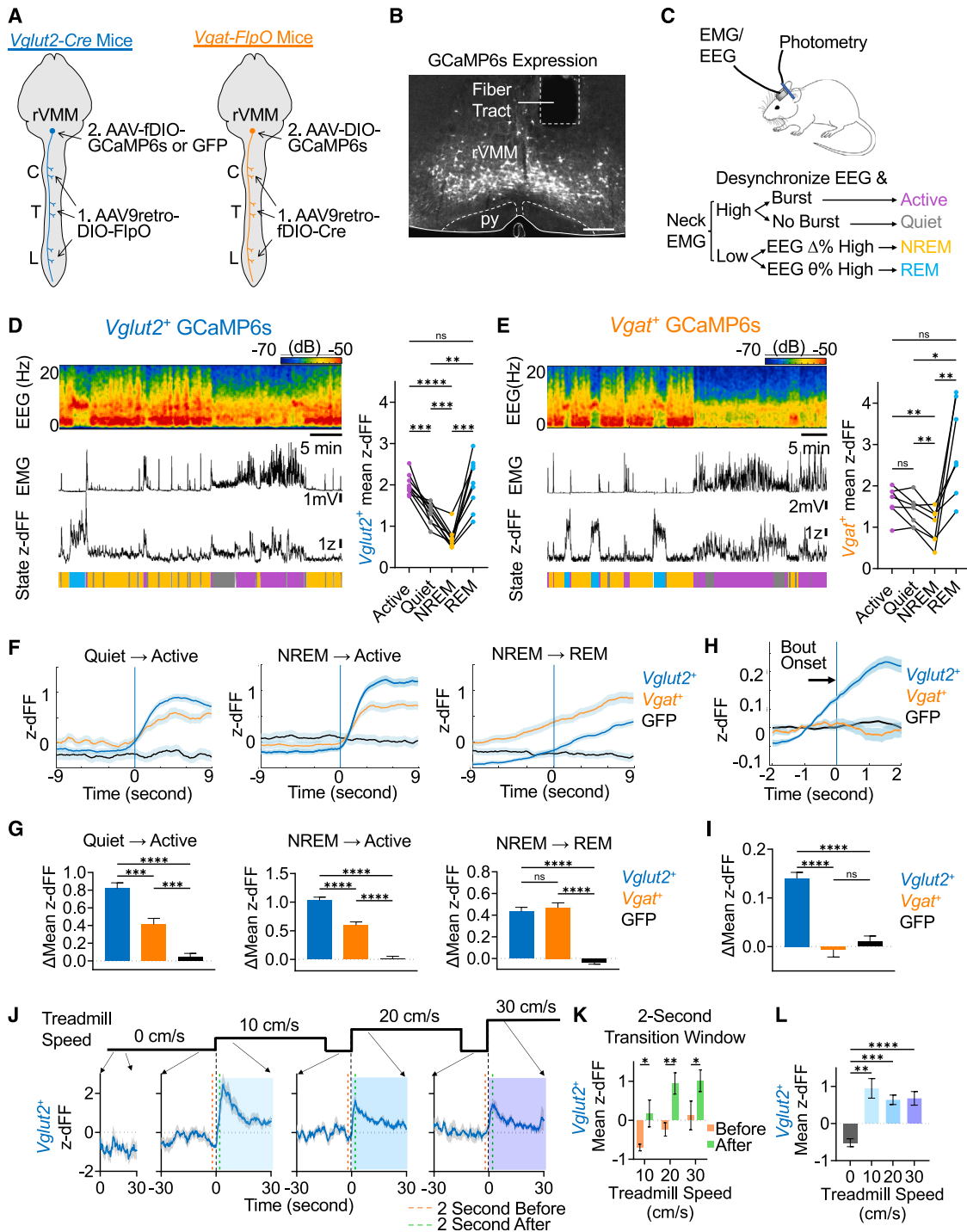
See also Figures S3 and S4.

Figure 5. Neuronal activity patterns of excitatory and inhibitory rVMM SPNs in different behavioral states

(A) Experimental scheme.

(B) Representative imaging of rVMM showing the excitatory rVMM SPNs expressing GCaMP6s and the fiber-optic tract. White rectangle indicates fiber-optic tract. Scale bars, 200 μm.

(C) Scheme showing EMG/EEG/Photometry recording of mice. Both EMG and EEG data were considered to define four different states (see text for details). Purple for active state, gray for quiet state, yellow for NREM state, and blue for REM state. The same color coding is used in the subsequent panels.

(D) Example recording and analysis of *Vglut2*+ rVMM SPNs calcium activity. Left: EEG spectrogram, EMG, and *Z* scored dFF. Corresponding arousal states were indicated at the bottom. Right: group comparison of *Vglut2*+ rVMM SPNs calcium activity between different states (mean ± SEM, *n* = 9). ****, *p* < 0.0001; ***, *p* < 0.001; **, *p* < 0.01; ns, not significant; repeated measures one-way ANOVA with Fisher's LSD multiple comparisons test.

(legend continued on next page)

home cage condition where mice could undergo sleep/awake cycles with associated activities such as sleep, rest, and locomotion, and (2) on a treadmill where mice were subjected to locomotion of different speeds. In parallel, we also recorded electroencephalogram (EEG) with electrodes on the skull and EMG from deep neck/anterior trunk muscles (Figure 5C).[52–54]

We first recorded these parameters over 7 h in the daytime when mice were kept in an open arena. By examining the Pearson correlation between different parameters, we found that the calcium signals of excitatory rVMM SPNs were positively correlated with EMG amplitude and EEG theta-band power density but negatively correlated with EEG delta-band power density (Figures S5A and S5D). No such correlation was found in GFP controls (Figures S5B and S5D). These results prompted us to analyze their neuronal activities in different arousal states, namely: (1) active: high EMG tone with burst firing and desynchronized EEG; (2) quiet: high EMG tone without burst firing and desynchronized EEG; (3) non-REM (NREM) sleep: low EMG tone with high EEG delta-band power density; and (4) REM sleep: further reduced EMG tone with high EEG theta-band power density and low delta-band density (Figure 5C). We found that the mean calcium signals of excitatory rVMM SPNs were highest in the active state, moderate in a quiet state, and low in NREM sleep (Figure 5D). On the other hand, the GFP signal in control animals did not change in these different arousal states (Figure S5E). Moreover, the activities of the excitatory neurons exhibited significant alteration at the transitions of different behavioral states (Figures 5F, 5G, and S5F), positively correlating with increased active/arousal states. No such alterations were observed in the GFP control group (Figures 5F, 5G, and S5F). In the active state, mice often undertook exploratory locomotion bouts.[55] We found that the calcium signals of these excitatory rVMM SPNs exhibited a modest yet significant increase at the onset of locomotion bouts (Figures 5H and 5I), suggesting that the activities of these neurons correlate with the initiation of locomotion bouts.

In another set of experiments, we monitored autonomic parameters together with EEG and EMG by implanting a telemetry device into the carotid artery in intact mice.[56] We found that the sympathetic tone, as measured by blood pressure and heart rate, varied similarly to the excitatory SPN activity (Figure S5G).

Intriguingly, calcium signals of excitatory rVMM SPNs increased in REM sleep (Figure 5D), despite muscle atonia in this state. This might be relevant to the muscle twitches and increased blood pressure observed in some REM sleep episodes.[57]

However, the calcium signals of inhibitory rVMM SPNs had a significantly weaker correlation to the neck muscle activity, even though they also showed a positive correlation with EEG theta-band power density and a negative correlation with EEG delta-band power density (Figures S5C and S5D). Their mean calcium signals were at moderate levels during active (with a few observable peaks during grooming, eating, and nesting) and quiet states, reached the lowest level in NREM sleep, and significantly surged in REM sleep (Figure 5E), suggesting that the inhibitory rVMM SPNs might have a role in regulating muscle atonia and autonomic suppression during REM sleep. Like the excitatory populations, the inhibitory SPNs exhibited significant alteration in activity at the transitions between different behavioral states yet had significantly lower activities during the active state (Figures 5F, 5G, and S5F). In addition, there is a downward trend of their activities associated with individual locomotion bouts in active states, but these changes did not reach statistical significance (Figures 5H and 5I). Because of modest activity changes and the short duration of individual bouts, further studies are needed to establish a precise relationship between the onset/offsets of bouts and these neuronal activities.

We next analyzed the neuronal activities of these SPNs when mice ran at different speeds on a treadmill. For the rVMM excitatory SPNs, the calcium signals were low when the mice were quiet (when the treadmill is off), similar to the observation in an open arena recording (Figure 5J, first panel). Their calcium signals became elevated when the treadmill was turned on regardless of the treadmill speed (Figures 5J, second to fourth panels, and 5K), suggesting that these neurons might be important for initiating high-speed locomotion. Consistent with excitatory SPN activity dynamics, the amplitude of neck EMGs increased during running and remained at comparable levels at different speeds (Figure S5H, left panel), while blood pressure also increased gradually (Figure S5H, right panel). On the other hand, the calcium signals of inhibitory rVMM SPNs slightly decreased during running at higher speed, while the control GFP signals of excitatory rVMM SPNs remained static (Figure S5I).

(E) Example recording and analysis of *Vgat*[+] rVMM SPNs calcium activity. Left: EEG spectrogram, EMG, and Z scored dFF. Corresponding arousal states were indicated at the bottom. Right: group comparison of *Vgat*[+] rVMM SPNs calcium activity between different states (mean ± SEM, n = 7). ****, $p < 0.0001$; ***, $p < 0.001$; **, $p < 0.01$; ns, not significant; repeated measures one-way ANOVA with Fisher's LSD multiple comparisons test.

(F) Calcium activities (z-dFF, mean ± SEM) of excitatory and inhibitory rVMM SPNs during transitions of different behavioral states. For *Vglut2*^{+} GCaMP6s, 9 mice were recorded, and n = 127 events for quiet to active (Q–A), n = 194 for NREM to active (N–A), n = 235 for NREM to REM (N–R); for *Vgat*[+] GCaMP6s, 7 mice were recorded, n = 105 events for Q–A, n = 160 for N–A, n = 167 for N–R; for GFP, N = 6 mice, n = 61 events for Q–A, n = 98 for N–A, and n = 132 for N–R.)

(G) Average (±SEM) of calcium activity changes (9 s post-transition minus 9 s pre-transition). ***, $p < 0.001$; ****, $p < 0.0001$; Kruskal-Wallis test with Dunn's multiple comparisons.

(H) Calcium activities (mean ± SEM) of excitatory and inhibitory rVMM SPNs during locomotion bout onset in open arena. Activities of 2 s before bout onset (>5 cm/s) were used as baseline.

(I) Comparison of calcium activities difference between each group. ns, not significant; ***, $p < 0.001$; ****, $p < 0.0001$; one-way ANOVA with Bonferroni comparison.

(J) Calcium activities (mean ± SEM) of *Vglut2*^{+} rVMM SPNs in treadmill running at different speeds. Average traces showing Z scored dFF in each treadmill speed. Time points of 2 s before and 2 s after treadmill onset are shown as break lines in orange and green, respectively. 30-s periods are shaded in blue. N = 7.

(K) Mean (±SEM) z-dFF of 2 s before and 2 s after treadmill onset at different speeds. *, $p < 0.05$; **, $p < 0.01$; paired t test.

(L) Mean (±SEM) z-dFF of 30 s after treadmill onset at different speeds, compared with the mean z-dFF during quiet moments (0). **, $p < 0.01$; mixed-effects analysis with Fisher's LSD multiple comparisons test.

See also Figure S5.
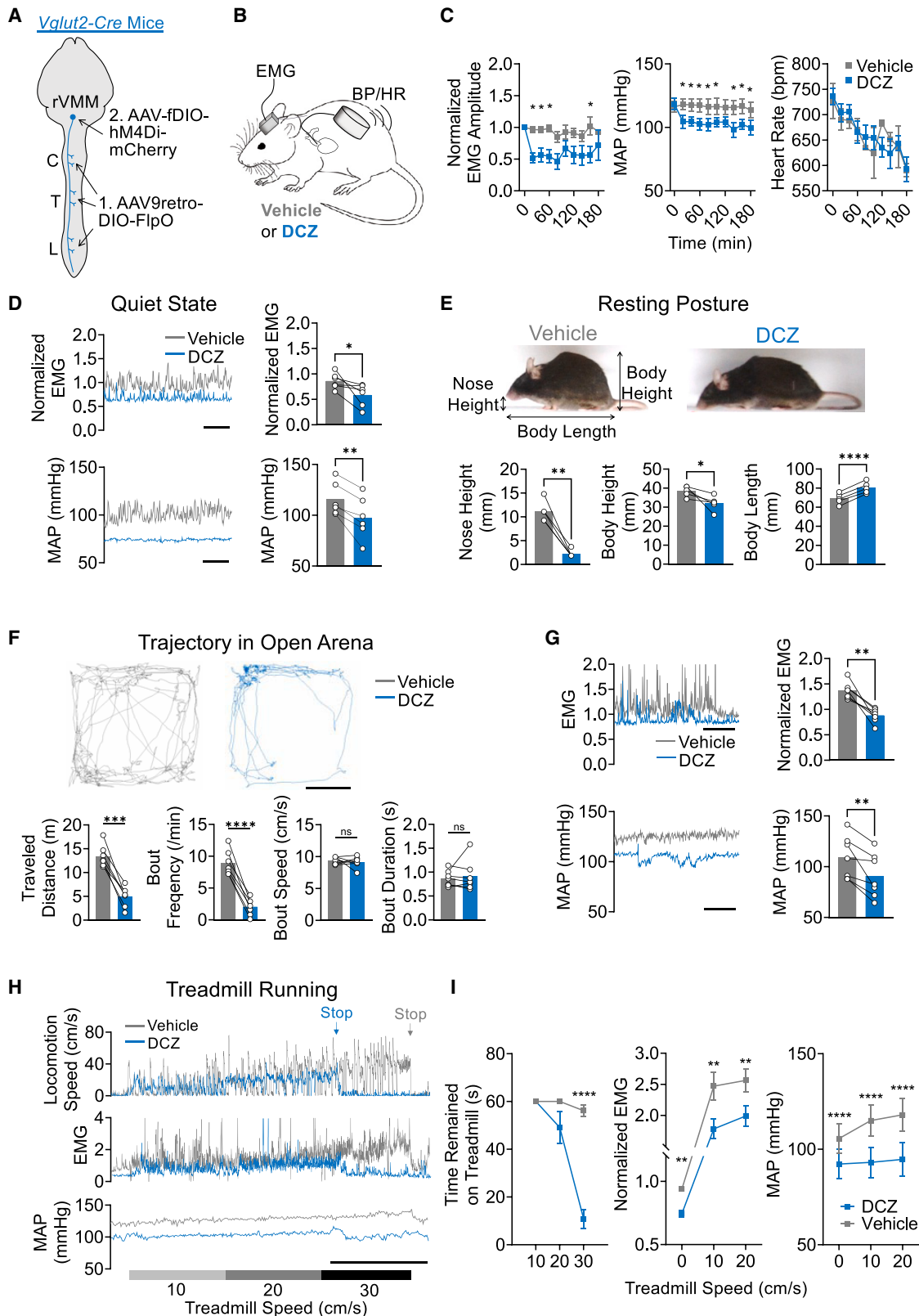
(legend on next page)

To complement the forced locomotion on a treadmill experiment, we performed additional experiments on mice performing voluntary running on a horizontal disc.[58] Similar to what was observed on the treadmill (Figures 5J–5L), the activities of excitatory SPNs increased at the transitions from non-locomotion to locomotion (0 to 10 cm/s; Figures S5J and S5R1) but did not increase further at higher speeds (>10 cm/s) (Figures S5J and S5R2). Similarly, blood pressure and heart rate dramatically increased when initiating running (0 to 10 cm/s) but increased less at higher speeds (>10 cm/s) (Figure S5K). These results suggest similar neuronal activities and blood pressure dynamics occur during voluntary locomotion (Figures S5J and S5K) and forced locomotion on the treadmill (Figures 5G, 5H, and 5J–5L). Our results suggest that the rVMM excitatory SPNs may be crucial in regulating proper levels of skeletal muscle and sympathetic tone to support increased locomotion and muscle contractility, perhaps by providing homeostatic and metabolic preparations.

Excitatory rVMM SPNs are required for setting both skeletal muscle and sympathetic tone during rest and locomotion

We next asked if these rVMM SPNs are required for the relevant behavior. We expressed the inhibitory receptor hM4Di in rVMM SPNs in *Vglut2-Cre* mice and silenced their activity by injecting the ligand deschlorocloʐapine (DCZ) (Figures 6A and S6A–S6C).[59] Because DCZ-triggered silencing lasts for only 2–3 h,[59] our studies focused on the active and quiet states in the home cage, as well as active locomotion in the open arena and treadmill. EMG and sympathetic functions (arterial blood pressure and heart rate) were monitored (Figure 6B). In the home cage condition, when mice are at rest, DCZ treatment significantly decreased EMG activity and blood pressure, not heart rate, in *Vglut2-Cre* mice (Figure 6C) but not in control mice (Figures S6F and S6G). The effect lasts about 3 h, correlating with the effective time of DCZ-mediated silencing (Figure S6D). Further analysis indicated that DCZ treatment reduced basal muscle tone and blood pressure in the quiet state (Figure 6D). It is striking that silencing excitatory rVMM SPNs

reduced resting blood pressure, differing from the previous study that found that silencing C1 neurons had little effect on basal blood pressure.[60] Consistently, we also noticed that DCZ-assisted silencing changed the animal's resting posture, as evidenced by reduced nose height, body height, and elongated body length (Figure 6E), likely reflecting the reduced muscle tone. However, this silencing did not significantly alter other locomotion parameters (Figure S6E).

In an open arena, DCZ treatment reduced total traveled distance and the frequency of active locomotion bouts in the Vglut2-Cre mice with hM4Di expression in rVMM SPNs (Figure 6F) but not in the control mice (Figure S6H), consistent with their activity patterns (Figure 5H). These silenced mice also exhibited reduced EMG and blood pressure (Figure 6G). Thus, excitatory rVMM SPNs might be important in setting basal levels of skeletal muscle and sympathetic tone for locomotion and exploratory behaviors. Furthermore, on the treadmill where mice were subjected to running at different speeds, DCZ treatment reduced the time the mice remained on the treadmill at 30 cm/s (Figures 6H, 6I, and S6I). Consistently, the silenced mice exhibited reduced levels of muscle activity and blood pressure at rest and failed to mobilize these functions with increased treadmill speeds (Figures 6H and 6I), suggesting that these excitatory rVMM SPNs are also required to support high-speed locomotion.

Inhibitory rVMM SPNs are required for muscle atonia and sympathetic suppression during REM sleep

Finally, we assessed the behavioral outcome of silencing inhibitory rVMM SPNs with a tetanus toxin light-chain (TeLC)-assisted method[61] (Figures 7A and S7A–S7C). In an open arena, mice with silenced inhibitory rVMM SPNs displayed increased activities (Figure 7B), evidenced by increased distance traveled and locomotion bout frequency and duration, but not speed (Figure 7C). These effects are opposite to what was seen after the silencing of excitatory rVMM SPNs (Figure 6). This is consistent with the observations that the inhibitory rVMM SPNs are at modest activity levels during awake (active and quiet) states (Figure 5).

Figure 6. Silencing excitatory rVMM SPNs reduces muscle and sympathetic tone at rest and during locomotion

(A) Experimental scheme.

(B) Scheme of EEG/EMG and blood pressure (BP)/heart rate (HR) recording in behaving mice.

(C) Dynamics (in 20-min time window right after vehicle or DCZ treatment) of EMG amplitude, MAP, and heart rate of mice in home cage. Zero represents baseline of 20 min prior to treatment. *, $p < 0.05$; $n = 7$; mixed-effects analysis with Bonferroni's multiple comparisons test.

(D) Representative EMG amplitude and MAP in quite state (left) and quantification (right) after vehicle or DCZ treatment. Scale bars, 60 s. Right: mean and individual value of EMG amplitude and MAP in quiet state after vehicle or DCZ treatment. *, $p < 0.05$; **, $p < 0.01$; paired t test.

(E) Images (upper) and quantification of body posture at rest after vehicle or DCZ treatment. For lower panel, quantification, mean, and individual value. *, $p < 0.05$; **, $p < 0.01$; ****, $p < 0.0001$; paired t test.

(F) Trajectory of body mass position for 10 min in open arena after vehicle or DCZ treatment (left) and quantification of performance in open arena (right). Scale bars, 10 cm. For the right panel, mean and individual value. ***, $p < 0.001$; ****, $p < 0.0001$; paired t test.

(G) Representative EMG amplitude and MAP in open arena after vehicle or DCZ treatment (left) and mean and individual value of EMG amplitude and MAP (right). Scale bars, 60 s. **, $p < 0.01$; paired t test.

(H) Representative traces of locomotion speed (top), normalized EMG (middle), and MAP (bottom) at different treadmill speeds after vehicle or DCZ treatment. Timescale bars, 60 s.

(I) Average (±SEM) locomotion speed, EMG peak amplitude, and MAP at different treadmill speeds after vehicle or DCZ treatment. The levels of EMG and MAP from vehicle controls were sub-sampled to match the duration of running in the DCZ group. **, $p < 0.01$, ****, $p < 0.0001$; $n = 7$; two-way ANOVA with Tukey's multiple comparisons test.

See also Figure S6.
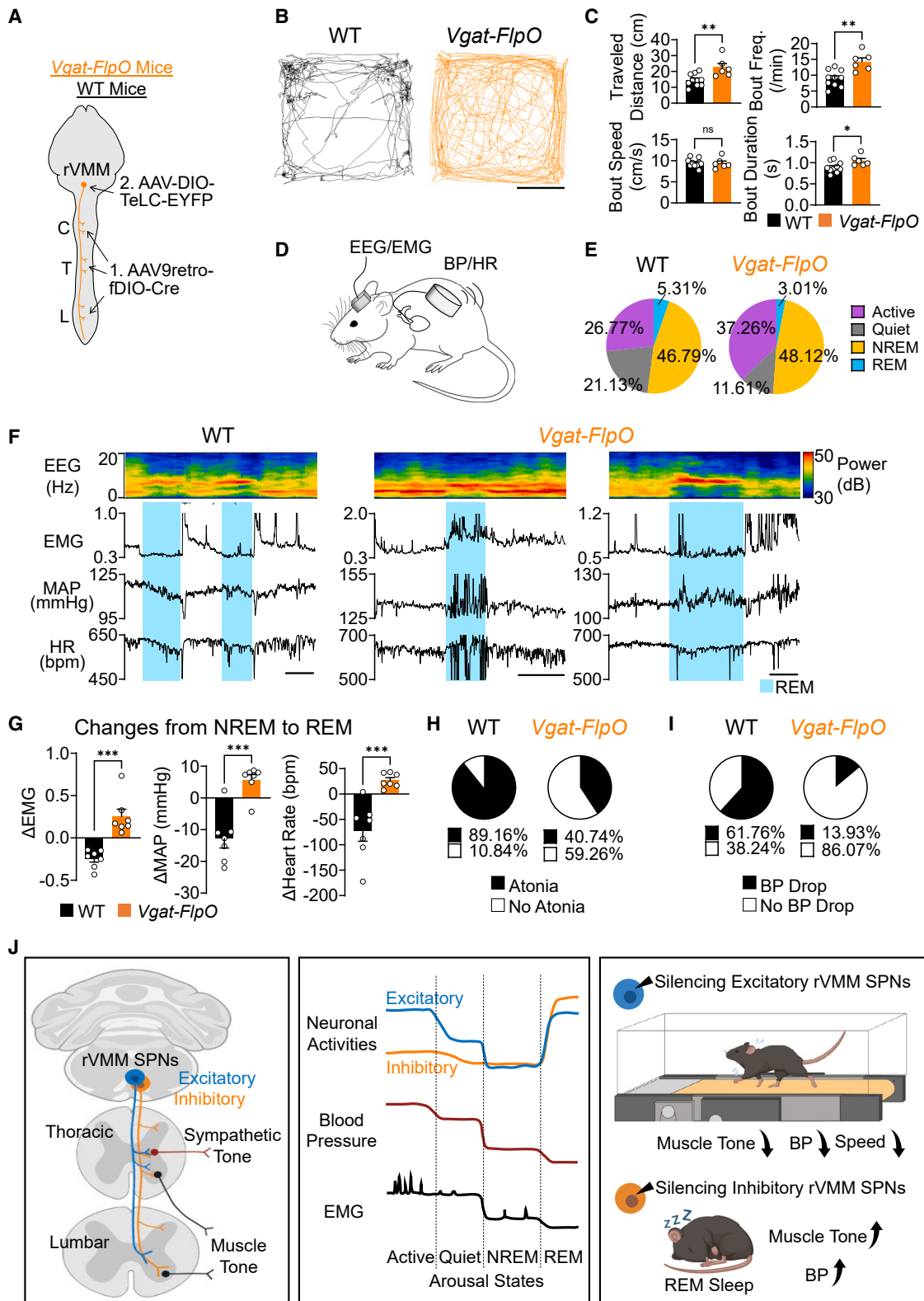
Next, we recorded EEG/EMG and sympathetic readouts when the mice were in the home cage condition (Figure 7D). Because rVMM SPN silencing might affect muscle activities, video tracking of body movements was also performed to assist the interrogation of the four arousal states: (1) active (desynchronized EEG, with movement), (2) quiet (desynchronized EEG, without movement), (3) NREM sleep (high delta, low theta, and no movement), and (4) REM sleep (low delta, high theta, and no movement). In the silenced group, the four behavioral states are still distinguishable (Figures S7D and S7E), but with increased total duration in the active state and decreased total duration in the quiet state compared with the wild-type control group (Figures 7E and S7F). Noticeably, several aspects of REM sleep were severely disrupted. First, the overall REM sleep duration was reduced in the silenced group (Figures 7E and S7F). Second, EMG level significantly increased with burst activities, accompanied by increased blood pressure and heart rate in the silenced group, in contrast to the low EMG level (muscle atonia) and the often-reduced blood pressure/heart rate during REM sleep episodes in controls (Figures 7F and 7G). Third, there was a significant reduction of tonic REM sleep episodes (complete muscle atonia and reduction of blood pressure and heart rate) in the silenced group, as opposed to the control group (Figures 7H, 7I, and S7G). These findings suggest that inhibitory rVMM SPNs are required for atonia and reduction of sympathetic outflow during REM sleep, consistent with the observation that these neurons are the most active during REM sleep (Figure 5). Our results reveal an important role for inhibitory rVMM SPNs in controlling both the somatomotor and sympathetic functions during REM sleep and awake states, correlating with their activity levels.

DISCUSSION

Multi-functioning SPNs in the rVMM

In mammals, there are several hundred skeletal muscles for somatic functions and many peripheral organs, including billions of smooth muscle cells as the effectors of sympathetic activities. In explaining how a small number of descending brain-spinal pathways achieve complex behavioral coordination, a plausible model is that individual behaviors in a hierarchical architecture are constructed by combining discrete building blocks.[62–64] As individual behaviors have shared and unique components of motor, sensory, and autonomic functions, distinct SPNs might control these functions separately, forming "function-specific" modules. This model could offer the maximal flexibility of control. Alternatively, certain SPNs could innervate multiple targets and control multiple functions. Such "multi-functional" modules may mobilize the behaviorally correlated functions simultaneously, increasing controlling efficiency with the cost of a reduced degree of freedom. Our functional mapping results suggest SPNs utilize both strategies. Several SPN populations, such as rubrospinal neurons and several populations of reticulospinal neurons, preferentially trigger somatic muscle activities, while the hypothalamospinal neurons in the PVN are more specific to sympathetic control.[17,38] By contrast, the excitatory and inhibitory SPNs in the rVMM are multi-functional and differentially regulate both the somatomotor and sympathetic responses. Extending from the notion that rVMM-derived reticulospinal neurons elaborate collaterals in the entire spinal cord,[46–50,65] our anatomical results suggest that these neurons possess multi-level collaterals innervating both the IML and distinct motor and even sensory regions in the spinal cord, along with several nuclei in the brainstem. Of note, the dorsal horn innervation by inhibitory SPNs suggests an additional role of this population in sensory processing, a hypothesis that remains to be tested, in addition to somatomotor and sympathetic controls. Thus, the multiple innervations and functions of these SPNs might underlie their properties as "command neurons" in translating brain-derived commands into different motor, sensory, and autonomic engagements that constitute complex behaviors.

The role of rVMM SPNs in arousal state control

Most behaviors depend on an animal's arousal state.[3,4] Our results reveal a remarkable correlation between the activation of both excitatory and inhibitory rVMM SPNs and different arousal states (Figure 7J). Excitatory SPNs' activities are positively correlated with EMG and theta-band EEG and negatively with delta-band EEG during these differential arousal states, except for paradoxical REM sleep. On the other hand, inhibitory SPNs are the most active in REM sleep, significantly less in an awake state, and the least active in NREM sleep. Interestingly, both populations are highly active in REM sleep. Although different mechanisms have been proposed for REM-associated atonia,[66,67] our results suggest inhibitory SPNs in the rVMM play a key role. These neurons directly innervate spinal motor neurons

---

Figure 7. Silencing inhibitory rVMM SPNs increases locomotion in awake mice and impairs muscle atonia and sympathetic reduction in REM sleep

(A) Experimental scheme.

(B) Representative body mass trajectories in open arena. Scale bars, 10 cm.

(C) Average (±SEM) of different parameters for locomotion in open arena, $n = 6$ for *Vgat-FlpO* mice, $n = 10$ for WT mice. *, $p < 0.05$; **, $p < 0.01$; ns, not significant; unpaired t test.

(D) Scheme of EEG/EMG and BP/HR recording in behaving mice.

(E) Mean proportion of four different behavioral states from 24-h recording in WT and *Vgat-FlpO* mice. Statistical differences are found in active and REM sleep states (Figure S7F). Percentage, mean ± SEM, $n = 7$, unpaired t test.

(F) Representative traces of EEG power spectrum, EMG amplitude, MAP, and HR in REM sleep episode in WT and *Vgat-FlpO* mice. Scale bar, 60 s.

(G) Average (±SEM) changes of EMG, MAP, and heart rate compared with preceding baseline (30 s prior to REM onset). ***, $p < 0.001$; unpaired t test.

(H and I) Proportion of REM sleep episodes with or without muscle (I) and proportion of REM sleep episodes with or without blood pressure drop (J) atonia in WT or *Vgat-FlpO* mice. Differences are statistically significant (Figure S7G).

(J) Summary of the key results.

See also Figure S7.

(Figure 4),[45] fitting with the expected role in triggering hyperpolarization in the spinal motor neurons.[68–70] These neurons also elaborate collaterals to several cranial nuclei but avoid the oculomotor nucleus and trochlear nucleus, which may explain the presence of eye movements during this stage of sleep. Furthermore, this inhibitory population heavily innervates the dorsal horn, possibly contributing to reduced sensory processing and awareness in REM sleep. However, the question remains: why does atonia persist during REM sleep even when these excitatory SPNs are activated? Unlike inhibitory SPNs, which directly hyperpolarize spinal motor neurons through direct innervation, excitatory SPNs primarily target pre-motor neurons rather than motor neurons themselves. This suggests that inhibitory SPNs could overpower the excitatory signals, keeping spinal motor neurons inactive.

Activation of excitatory SPNs in rVMM sets the competence for high-speed locomotion

An obvious example of somatic and autonomic coordination is high-speed locomotion or exercise. Classic studies demonstrated that in decorticate and paralyzed cats, cardiovascular variables increase during fictive locomotion.[71] In addition, stimulation of the mesencephalic locomotor region (MLR) leads to co-recruitment of locomotion and autonomic functions.[72–74] Our results suggest that SPNs in the rVMM might be a potential substrate for such coordination. In particular, silencing excitatory SPNs in rVMM not only reduced basal muscle tone and blood pressure at rest but also abolished the speed-dependent increase of blood pressure and mobilization of somatic muscle activation. However, these SPNs in the rVMM do not exhibit speed-dependent further activation, suggesting that other mechanisms account for the speed-dependent recruitment of motor and autonomic functions. Together, these results suggest that the activities of these reticulospinal neurons define the behavioral competence for both basic and demanding motor performance. This competence consists of both the somatomotor and sympathetic arms. The somatomotor arm mainly controls the skeletal muscle tone, an essential component of posture-gait control.[26,75] On the other hand, the sympathetic arm regulates relevant homeostatic and metabolic states conducive to different behaviors and physiological needs. In various behavioral contexts, these SPNs in rVMM might be regulated by cognition- or emotion-dependent signals from the higher levels of the brain. Future studies will determine how these and other SPNs coordinate and control the planning and execution of individual bodily behaviors.

Limitations of the study

Although our studies analyzed excitatory and inhibitory SPNs in rVMM, these neurons might not be homogenous. Molecularly, our single nuclei RNAseq analysis revealed distinct populations of SPNs in the medulla.[34] Anatomically, although we showed that the SPNs labeled from L4/5 spinal segments innervate the entire spinal cord, the co-injection of AAV9-H2B-tdTomato in L4/5 may underestimate the diffusion of Cre or FlpO viruses, considering that the transduction necessary for fluorophore expression is typically higher than that for recombinase activity. We cannot rule out the possibility that subsets of SPNs preferentially innervate some spinal segments. Functionally, our fiber-photometry recording collected the activity of neuronal populations and cannot distinguish sub-populations or individual neuronal activities correlated to other aspects of behaviors. In addition, due to the relatively slow kinetics of GCaMP6s, it is difficult to establish a precise temporal relationship between the activity of rVMM SPNs and some aspects of behaviors. Furthermore, despite the demonstrated link between these SPNs and different behavioral states, we do not know how these neurons' activities are regulated. Future studies will investigate the pre-synaptic inputs to these SPNs to understand their specific roles across various physiological and pathological conditions, such as spinal cord injury and stroke.

STAR★METHODS

Detailed methods are provided in the online version of this paper and include the following:

- KEY RESOURCES TABLE
- RESOURCE AVAILABILITY
  - Lead contact
  - Materials availability
  - Data and code availability
- EXPERIMENTAL MODEL AND STUDY PARTICIPANT DETAILS
  - Mouse Strains
- METHOD DETAILS
  - Virus production and injection
  - Opto-stimulation, EMG and blood pressure recording in anesthetized mice
  - Chronic recording of autonomic, EEG and EMG in behaving mice
  - Fiber photometry recording on rVMM SPNs
  - Behavioral tests
  - Slice recording on sympathetic preganglionic neurons in thoracic spinal cord
  - Immunohistochemistry
  - Imaging and histological analysis
- QUANTIFICATION AND STATISTICAL ANALYSIS

AUTHOR CONTRIBUTIONS

Z.Z., J.S., and Z.H. conceived and designed the experiments; Z.Z. performed acute and chronic *in vivo* recording experiments and data analysis; J.S., Z.Z., Y.L., and E.K. performed fiber-photometry recording and data analysis; Z.Z., J.T., and J.S. performed virus injections, chronic blood pressure recording, and behavioral assessments; Z.Z., J.S., J.C.P., C.C.W., Y.L., S.C., X.Y., and Y.Y. performed imaging and anatomical analysis; L.C. and Z.Z. performed slice recording and data analysis; Y.Z., J.B., J.I.C., C.Y.H., Z.Y., and S.C. participated in data analysis; Z.Z., J.S., C.C.W., and Z.H. prepared the manuscript with the inputs from all authors.

DECLARATION OF INTERESTS

Z.H. is a co-founder of Rugen and Myrobalan and an advisor of Axonis.

REFERENCES

1. Waldrop, T.G., Eldridge, F.L., Iwamoto, G.A., and Mitchell, J.H. (2010). Central neural control of respiration and circulation during exercise. Comprehensive physiology, pp. 333–380.

2. Michelini, L.C., O'Leary, D.S., Raven, P.B., and Nóbrega, A.C.L. (2015). Neural control of circulation and exercise: a translational approach disclosing interactions between central command, arterial baroreflex, and muscle metaboreflex. Am. J. Physiol. Heart Circ. Physiol. 309, H381–H392. https://doi.org/10.1152/ajpheart.00077.2015.

3. Liu, D., and Dan, Y. (2019). A Motor Theory of Sleep-Wake Control: Arousal-Action Circuit. Annu. Rev. Neurosci. 42, 27–46. https://doi.org/10.1146/annurev-neuro-080317-061813.

4. Scammell, T.E., Arrigoni, E., and Lipton, J.O. (2017). Neural Circuitry of Wakefulness and Sleep. Neuron 93, 747–765. https://doi.org/10.1016/j.neuron.2017.01.014.

5. Strack, A.M., Sawyer, W.B., Marubio, L.M., and Loewy, A.D. (1988). Spinal origin of sympathetic preganglionic neurons in the rat. Brain Res. 455, 187–191. https://doi.org/10.1016/0006-8993(88)90132-1.

6. Swanson, L.W., and Mogenson, G.J. (1981). Neural mechanisms for the functional coupling of autonomic, endocrine and somatomotor responses in adaptive behavior. Brain Res. 228, 1–34. https://doi.org/10.1016/0165-0173(81)90010-2.

7. Miki, K., and Yoshimoto, M. (2013). Sympathetic nerve activity during sleep, exercise, and mental stress. Auton. Neurosci. 174, 15–20. https://doi.org/10.1016/j.autneu.2012.12.007.

8. Barman, S.M., and Yates, B.J. (2017). Deciphering the Neural Control of Sympathetic Nerve Activity: Status Report and Directions for Future Research. Front. Neurosci. 11, 730. https://doi.org/10.3389/fnins.2017.00730.

9. Cowley, K.C. (2018). A new conceptual framework for the integrated neural control of locomotor and sympathetic function: implications for exercise after spinal cord injury. Appl. Physiol. Nutr. Metab. 43, 1140–1150. https://doi.org/10.1139/apnm-2018-0310.

10. Courtine, G., and Sofroniew, M.V. (2019). Spinal cord repair: advances in biology and technology. Nat. Med. 25, 898–908. https://doi.org/10.1038/s41591-019-0475-6.

11. Fouad, K., Popovich, P.G., Kopp, M.A., and Schwab, J.M. (2021). The neuroanatomical-functional paradox in spinal cord injury. Nat. Rev. Neurol. 17, 53–62. https://doi.org/10.1038/s41582-020-00436-x.

12. Eldahan, K.C., and Rabchevsky, A.G. (2018). Autonomic dysreflexia after spinal cord injury: Systemic pathophysiology and methods of management. Auton. Neurosci. 209, 59–70. https://doi.org/10.1016/j.autneu.2017.05.002.

13. Gandevia, S.C., Killian, K., McKenzie, D.K., Crawford, M., Allen, G.M., Gorman, R.B., and Hales, J.P. (1993). Respiratory sensations, cardiovascular control, kinaesthesia and transcranial stimulation during paralysis in humans. J. Physiol. 470, 85–107. https://doi.org/10.1113/jphysiol.1993.sp019849.

14. Goodwin, G.M., McCloskey, D.I., and Mitchell, J.H. (1972). Cardiovascular and respiratory responses to changes in central command during isometric exercise at constant muscle tension. J. Physiol. 226, 173–190. https://doi.org/10.1113/jphysiol.1972.sp009979.

15. Asmussen, E., Johansen, S.H., Jorgensen, M., and Nielsen, M. (1965). On the Nervous Factors Controlling Respiration and Circulation during Exercise. Experiments with Curarization. Acta Physiol. Scand. 63, 343–350. https://doi.org/10.1111/j.1748-1716.1965.tb04073.x.

16. Liang, H., Paxinos, G., and Watson, C. (2011). Projections from the brain to the spinal cord in the mouse. Brain Struct. Funct. 215, 159–186. https://doi.org/10.1007/s00429-010-0281-x.

17. Lemon, R.N. (2008). Descending pathways in motor control. Annu. Rev. Neurosci. 31, 195–218. https://doi.org/10.1146/annurev.neuro.31.060407.125547.

18. Brownstone, R.M., and Chopek, J.W. (2018). Reticulospinal Systems for Tuning Motor Commands. Front. Neural Circuits 12, 30. https://doi.org/10.3389/fncir.2018.00030.

19. Perreault, M.C., and Giorgi, A. (2019). Diversity of reticulospinal systems in mammals. Curr. Opin. Physiol. 8, 161–169. https://doi.org/10.1016/j.cophys.2019.03.001.

20. Guyenet, P.G. (2006). The sympathetic control of blood pressure. Nat. Rev. Neurosci. 7, 335–346. https://doi.org/10.1038/nrn1902.

21. Souza, G.M.P.R., Stornetta, R.L., Stornetta, D.S., Guyenet, P.G., and Abbott, S.B.G. (2022). Adrenergic C1 neurons monitor arterial blood pressure and determine the sympathetic response to hemorrhage. Cell Rep. 38, 110480. https://doi.org/10.1016/j.celrep.2022.110480.

22. Guyenet, P.G., Stornetta, R.L., Bochorishvili, G., Depuy, S.D., Burke, P.G.R., and Abbott, S.B.G. (2013). C1 neurons: the body's EMTs. Am. J. Physiol. Regul. Integr. Comp. Physiol. 305, R187–R204. https://doi.org/10.1152/ajpregu.00054.2013.

23. Arber, S., and Costa, R.M. (2018). Connecting neuronal circuits for movement. Science 360, 1403–1404. https://doi.org/10.1126/science.aat5994.

24. Leiras, R., Cregg, J.M., and Kiehn, O. (2022). Brainstem Circuits for Locomotion. Annu. Rev. Neurosci. 45, 63–85. https://doi.org/10.1146/annurev-neuro-082321-025137.

25. Azim, E., and Alstermark, B. (2015). Skilled forelimb movements and internal copy motor circuits. Curr. Opin. Neurobiol. 33, 16–24. https://doi.org/10.1016/j.conb.2014.12.009.

26. Takakusaki, K. (2013). Neurophysiology of gait: from the spinal cord to the frontal lobe. Mov. Disord. 28, 1483–1491. https://doi.org/10.1002/mds.25669.

27. Deliagina, T.G., Zelenin, P.V., and Orlovsky, G.N. (2012). Physiological and circuit mechanisms of postural control. Curr. Opin. Neurobiol. 22, 646–652. https://doi.org/10.1016/j.conb.2012.03.002.

28. Liu, Y., Latremoliere, A., Li, X., Zhang, Z., Chen, M., Wang, X., Fang, C., Zhu, J., Alexandre, C., Gao, Z., et al. (2018). Touch and tactile neuropathic pain sensitivity are set by corticospinal projections. Nature 561, 547–550. https://doi.org/10.1038/s41586-018-0515-2.

29. Watakabe, A., Ohtsuka, M., Kinoshita, M., Takaji, M., Isa, K., Mizukami, H., Ozawa, K., Isa, T., and Yamamori, T. (2015). Comparative analyses of adeno-associated viral vector serotypes 1, 2, 5, 8 and 9 in marmoset, mouse and macaque cerebral cortex. Neurosci. Res. 93, 144–157. https://doi.org/10.1016/j.neures.2014.09.002.

30. Tervo, D.G.R., Hwang, B.Y., Viswanathan, S., Gaj, T., Lavzin, M., Ritola, K.D., Lindo, S., Michael, S., Kuleshova, E., Ojala, D., et al. (2016). A Designer AAV Variant Permits Efficient Retrograde Access to Projection Neurons. Neuron 92, 372–382. https://doi.org/10.1016/j.neuron.2016.09.021.

31. Gianino, S., Stein, S.A., Li, H., Lu, X., Biesiada, E., Ulas, J., and Xu, X.M. (1999). Postnatal growth of corticospinal axons in the spinal cord of developing mice. Brain Res. Dev. Brain Res. 112, 189–204. https://doi.org/10.1016/s0165-3806(98)00168-0.

32. O'Leary, D.D., and Koester, S.E. (1993). Development of projection neuron types, axon pathways, and patterned connections of the mammalian cortex. Neuron 10, 991–1006. https://doi.org/10.1016/0896-6273(93)90049-w.

33. Ganley, R.P., Werder, K., Wildner, H., and Zeilhofer, H.U. (2021). Spinally projecting noradrenergic neurons of the locus coeruleus display resistance to AAV2retro-mediated transduction. Mol. Pain 17, 17448069211037887. https://doi.org/10.1177/17448069211037887.

34. Winter, C.C., Jacobi, A., Su, J., Chung, L., van Velthoven, C.T.J., Yao, Z., Lee, C., Zhang, Z., Yu, S., Gao, K., et al. (2023). A transcriptomic taxonomy of mouse brain-wide spinal projecting neurons. Nature 624, 403–414. https://doi.org/10.1038/s41586-023-06817-8.

35. Vong, L., Ye, C., Yang, Z., Choi, B., Chua, S., Jr., and Lowell, B.B. (2011). Leptin action on GABAergic neurons prevents obesity and reduces inhibitory tone to POMC neurons. Neuron 71, 142–154. https://doi.org/10.1016/j.neuron.2011.05.028.

36. Burke, P.G.R., Li, Q., Costin, M.L., McMullan, S., Pilowsky, P.M., and Goodchild, A.K. (2008). Somatostatin 2A receptor-expressing presympathetic neurons in the rostral ventrolateral medulla maintain blood pressure. Hypertension 52, 1127–1133. https://doi.org/10.1161/HYPERTENSIONAHA.108.118224.

37. Ross, C.A., Ruggiero, D.A., Park, D.H., Joh, T.H., Sved, A.F., Fernandez-Pardal, J., Saavedra, J.M., and Reis, D.J. (1984). Tonic vasomotor control by the rostral ventrolateral medulla: effect of electrical or chemical stimulation of the area containing C1 adrenaline neurons on arterial pressure, heart rate, and plasma catecholamines and vasopressin. J. Neurosci. 4, 474–494. https://doi.org/10.1523/JNEUROSCI.04-02-00474.1984.

38. Saper, C.B., Loewy, A.D., Swanson, L.W., and Cowan, W.M. (1976). Direct hypothalamo-autonomic connections. Brain Res. 117, 305–312. https://doi.org/10.1016/0006-8993(76)90738-1.

39. Strack, A.M., Sawyer, W.B., Hughes, J.H., Platt, K.B., and Loewy, A.D. (1989). A general pattern of CNS innervation of the sympathetic outflow demonstrated by transneuronal pseudorabies viral infections. Brain Res. 491, 156–162. https://doi.org/10.1016/0006-8993(89)90098-x.

40. Dampney, R.A.L. (2015). Central mechanisms regulating coordinated cardiovascular and respiratory function during stress and arousal. Am. J. Physiol. Regul. Integr. Comp. Physiol. 309, R429–R443. https://doi.org/10.1152/ajpregu.00051.2015.

41. Savitt, J.M., Jang, S.S., Mu, W., Dawson, V.L., and Dawson, T.M. (2005). Bcl-x is required for proper development of the mouse substantia nigra. J. Neurosci. 25, 6721–6728. https://doi.org/10.1523/JNEUROSCI.0760-05.2005.

42. Squair, J.W., Gautier, M., Mahe, L., Soriano, J.E., Rowald, A., Bichat, A., Cho, N., Anderson, M.A., James, N.D., Gandar, J., et al. (2021). Neuroprosthetic baroreflex controls haemodynamics after spinal cord injury. Nature 590, 308–314. https://doi.org/10.1038/s41586-020-03180-w.

43. Daigle, T.L., Madisen, L., Hage, T.A., Valley, M.T., Knoblich, U., Larsen, R.S., Takeno, M.M., Huang, L., Gu, H., Larsen, R., et al. (2018). A Suite of Transgenic Driver and Reporter Mouse Lines with Enhanced Brain-Cell-Type Targeting and Functionality. Cell 174, 465–480.e22. https://doi.org/10.1016/j.cell.2018.06.035.

44. Goetz, C., Pivetta, C., and Arber, S. (2015). Distinct limb and trunk premotor circuits establish laterality in the spinal cord. Neuron 85, 131–144. https://doi.org/10.1016/j.neuron.2014.11.024.

45. Capelli, P., Pivetta, C., Soledad Esposito, M., and Arber, S. (2017). Locomotor speed control circuits in the caudal brainstem. Nature 551, 373–377. https://doi.org/10.1038/nature24064.

46. Martin, G.F., Humbertson, A.O., Laxson, C., and Panneton, W.M. (1979). Evidence for direct bulbospinal projections to laminae IX, X and the intermediolateral cell column. Studies using axonal transport techniques in the North American opossum. Brain Res. 170, 165–171. https://doi.org/10.1016/0006-8993(79)90948-x.

47. Zemlan, F.P., Behbehani, M.M., and Beckstead, R.M. (1984). Ascending and descending projections from nucleus reticularis magnocellularis and nucleus reticularis gigantocellularis: an autoradiographic and horseradish peroxidase study in the rat. Brain Res. 292, 207–220. https://doi.org/10.1016/0006-8993(84)90757-1.

48. Martin, G.F., Vertes, R.P., and Waltzer, R. (1985). Spinal projections of the gigantocellular reticular formation in the rat. Evidence for projections from different areas to laminae I and II and lamina IX. Exp. Brain Res. 58, 154–162. https://doi.org/10.1007/BF00238963.

49. Holstege, J.C., and Kuypers, H.G. (1987). Brainstem projections to spinal motoneurons: an update. Neuroscience 23, 809–821. https://doi.org/10.1016/0306-4522(87)90160-6.

50. Allen, G.V., and Cechetto, D.F. (1994). Serotoninergic and nonserotoninergic neurons in the medullary raphe system have axon collateral projections to autonomic and somatic cell groups in the medulla and spinal cord. J. Comp. Neurol. 350, 357–366. https://doi.org/10.1002/cne.903500303.

51. Lerner, T.N., Shilyansky, C., Davidson, T.J., Evans, K.E., Beier, K.T., Zalocusky, K.A., Crow, A.K., Malenka, R.C., Luo, L., Tomer, R., and Deisseroth, K. (2015). Intact-Brain Analyses Reveal Distinct Information Carried by SNc Dopamine Subcircuits. Cell 162, 635–647. https://doi.org/10.1016/j.cell.2015.07.014.

52. Prerau, M.J., Brown, R.E., Bianchi, M.T., Ellenbogen, J.M., and Purdon, P.L. (2017). Sleep Neurophysiological Dynamics Through the Lens of Multitaper Spectral Analysis. Physiology (Bethesda) 32, 60–92. https://doi.org/10.1152/physiol.00062.2015.

53. Thomson, D.J. (1982). Spectrum estimation and harmonic analysis. Proc. IEEE 70, 1055–1096. https://doi.org/10.1109/PROC.1982.12433.

54. Del Percio, C., Drinkenburg, W., Lopez, S., Infarinato, F., Bastlund, J.F., Laursen, B., Pedersen, J.T., Christensen, D.Z., Forloni, G., Frasca, A., et al. (2017). On-going electroencephalographic rhythms related to cortical arousal in wild-type mice: the effect of aging. Neurobiol Aging 49, 20–30. https://doi.org/10.1016/j.neurobiolaging.2016.09.004.

55. Ruder, L., Takeoka, A., and Arber, S. (2016). Long-Distance Descending Spinal Neurons Ensure Quadrupedal Locomotor Stability. Neuron 92, 1063–1078. https://doi.org/10.1016/j.neuron.2016.10.032.

56. Knot, H.J., and Lee, D. (2016). A Novel Freely Moving Animal Based Blood Pressure, ECG, and Dual Body Temperature Telemetry System for Group Housed Mice in Social Context. The FASEB J. 30, lb595. https://doi.org/10.1096/fasebj.30.1_supplement.lb595.

57. Chase, M.H., and Morales, F.R. (1990). The atonia and myoclonia of active (REM) sleep. Annu. Rev. Psychol. 41, 557–584. https://doi.org/10.1146/annurev.ps.41.020190.003013.

58. Novak, C.M., Burghardt, P.R., and Levine, J.A. (2012). The use of a running wheel to measure activity in rodents: relationship to energy balance, general activity, and reward. Neurosci. Biobehav. Rev. 36, 1001–1014. https://doi.org/10.1016/j.neubiorev.2011.12.012.

59. Nagai, Y., Miyakawa, N., Takuwa, H., Hori, Y., Oyama, K., Ji, B., Takahashi, M., Huang, X.P., Slocum, S.T., DiBerto, J.F., et al. (2020). Deschloroclozapine, a potent and selective chemogenetic actuator enables rapid neuronal and behavioral modulations in mice and monkeys. Nat. Neurosci. 23, 1157–1167. https://doi.org/10.1038/s41593-020-0661-3.

60. Wenker, I.C., Abe, C., Viar, K.E., Stornetta, D.S., Stornetta, R.L., and Guyenet, P.G. (2017). Blood Pressure Regulation by the Rostral Ventrolateral Medulla in Conscious Rats: Effects of Hypoxia, Hypercapnia, Baroreceptor Denervation, and Anesthesia. J. Neurosci. 37, 4565–4583.

61. Zhang, Y., Zhao, S., Rodriguez, E., Takatoh, J., Han, B.X., Zhou, X., and Wang, F. (2015). Identifying local and descending inputs for primary sensory neurons. J. Clin. Invest. 125, 3782–3794. https://doi.org/10.1172/JCI81156.

62. Tresch, M.C., Saltiel, P., and Bizzi, E. (1999). The construction of movement by the spinal cord. Nat. Neurosci. 2, 162–167. https://doi.org/10.1038/5721.

63. Tsetlin, M.L.v. (1973). Automaton Theory and Modeling of Biological Systems (Academic Press).

64. Arbib, M.A. (2011). Perceptual structures and distributed motor control. Comprehensive physiology, pp. 1449–1480.

65. Peterson, B.W., Maunz, R.A., Pitts, N.G., and Mackel, R.G. (1975). Patterns of projection and branching of reticulospinal neurons. Exp. Brain Res. 23, 333–351. https://doi.org/10.1007/BF00238019.

66. Weber, F., and Dan, Y. (2016). Circuit-based interrogation of sleep control. Nature 538, 51–59. https://doi.org/10.1038/nature19773.

67. Peever, J., and Fuller, P.M. (2017). The Biology of REM Sleep. Curr. Biol. 27, R1237–R1248. https://doi.org/10.1016/j.cub.2017.10.026.

68. Morales, F.R., Boxer, P., and Chase, M.H. (1987). Behavioral state-specific inhibitory postsynaptic potentials impinge on cat lumbar motoneurons during active sleep. Exp. Neurol. 98, 418–435. https://doi.org/10.1016/0014-4886(87)90252-4.

69. Soja, P.J., Morales, F.R., Baranyi, A., and Chase, M.H. (1987). Effect of inhibitory amino acid antagonists on IPSPs induced in lumbar motoneurons upon stimulation of the nucleus reticularis gigantocellularis during active sleep. Brain Res. 423, 353–358. https://doi.org/10.1016/0006-8993(87)90862-6.

70. Holstege, J.C. (1996). The ventro-medial medullary projections to spinal motoneurons: ultrastructure, transmitters and functional aspects. Prog. Brain Res. 107, 159–181. https://doi.org/10.1016/s0079-6123(08)61864-6.

71. Eldridge, F.L., Millhorn, D.E., and Waldrop, T.G. (1981). Exercise hyperpnea and locomotion: parallel activation from the hypothalamus. Science 211, 844–846. https://doi.org/10.1126/science.7466362.

72. Noga, B.R., and Whelan, P.J. (2022). The Mesencephalic Locomotor Region: Beyond Locomotor Control. Front. Neural Circuits 16, 884785. https://doi.org/10.3389/fncir.2022.884785.

73. Koba, S., Kumada, N., Narai, E., Kataoka, N., Nakamura, K., and Watanabe, T. (2022). A brainstem monosynaptic excitatory pathway that drives locomotor activities and sympathetic cardiovascular responses. Nat. Commun. 13, 5079. https://doi.org/10.1038/s41467-022-32823-x.

74. Goñi-Erro, H., Selvan, R., Caggiano, V., Leiras, R., and Kiehn, O. (2023). Pedunculopontine Chx10(+) neurons control global motor arrest in mice. Nat. Neurosci. 26, 1516–1528. https://doi.org/10.1038/s41593-023-01396-3.

75. Takakusaki, K., Saitoh, K., Harada, H., and Kashiwayanagi, M. (2004). Role of basal ganglia-brainstem pathways in the control of motor behaviors. Neurosci. Res. 50, 137–151. https://doi.org/10.1016/j.neures.2004.06.015.

76. Lin, J.Y., Knutsen, P.M., Muller, A., Kleinfeld, D., and Tsien, R.Y. (2013). ReaChR: a red-shifted variant of channelrhodopsin enables deep transcranial optogenetic excitation. Nat Neurosci 16, 1499–1508. https://doi.org/10.1038/nn.3502.

77. Zingg, B., Chou, X.L., Zhang, Z.G., Mesik, L., Liang, F., Tao, H.W., and Zhang, L.I. (2017). AAV-Mediated Anterograde Transsynaptic Tagging: Mapping Corticocollicular Input-Defined Neural Pathways for Defense Behaviors. Neuron 93, 33–47. https://doi.org/10.1016/j.neuron.2016.11.045.

78. Klapoetke, N.C., Murata, Y., Kim, S.S., Pulver, S.R., Birdsey-Benson, A., Cho, Y.K., Morimoto, T.K., Chuong, A.S., Carpenter, E.J., Tian, Z., et al. (2014). Independent optical excitation of distinct neural populations. Nat Methods 11, 338–346. https://doi.org/10.1038/nmeth.2836.

79. Schneeberger, M., Parolari, L., Das Banerjee, T., Bhave, V., Wang, P., Patel, B., Topilko, T., Wu, Z., Choi, C.H.J., Yu, X., et al. (2019). Regulation of Energy Expenditure by Brainstem GABA Neurons. Cell. https://doi.org/10.1016/j.cell.2019.05.048.

80. Beier, K.T., Steinberg, E.E., DeLoach, K.E., Xie, S., Miyamichi, K., Schwarz, L., Gao, X.J., Kremer, E.J., Malenka, R.C., and Luo, L. (2015). Circuit Architecture of VTA Dopamine Neurons Revealed by Systematic Input-Output Mapping. Cell 162, 622–634. https://doi.org/10.1016/j.cell.2015.07.015.

81. Chen, T.W., Wardill, T.J., Sun, Y., Pulver, S.R., Renninger, S.L., Baohan, A., Schreiter, E.R., Kerr, R.A., Orger, M.B., Jayaraman, V., et al. (2013). Ultrasensitive fluorescent proteins for imaging neuronal activity. Nature 499, 295–300. https://doi.org/10.1038/nature12354.

82. Runegaard, A.H., Sorensen, A.T., Fitzpatrick, C.M., Jorgensen, S.H., Petersen, A.V., Hansen, N.W., Weikop, P., Andreasen, J.T., Mikkelsen, J.D., Perrier, J.F., et al. (2018). Locomotor- and Reward-Enhancing Effects of Cocaine Are Differentially Regulated by Chemogenetic Stimulation of Gi-Signaling in Dopaminergic Neurons. eNeuro 5. https://doi.org/10.1523/ENEURO.0345-17.2018.

83. Economo, M.N., Viswanathan, S., Tasic, B., Bas, E., Winnubst, J., Menon, V., Graybuck, L.T., Nguyen, T.N., Smith, K.A., Yao, Z., et al. (2018). Distinct descending motor cortex pathways and their roles in movement. Nature 563, 79–84. https://doi.org/10.1038/s41586-018-0642-9.

84. Bankhead, P., Loughrey, M.B., Fernández, J.A., Dombrowski, Y., McArt, D.G., Dunne, P.D., McQuaid, S., Gray, R.T., Murray, L.J., Coleman, H.G., et al. (2017). QuPath: Open source software for digital pathology image analysis. Sci. Rep. 7, 16878. https://doi.org/10.1038/s41598-017-17204-5.

85. Mathis, A., Mamidanna, P., Cury, K.M., Abe, T., Murthy, V.N., Mathis, M.W., and Bethge, M. (2018). DeepLabCut: markerless pose estimation of user-defined body parts with deep learning. Nat. Neurosci. 21, 1281–1289. https://doi.org/10.1038/s41593-018-0209-y.

86. Paxinos, G., and Franklin, K.B. (2019). Paxinos and Franklin's the Mouse Brain in Stereotaxic Coordinates (Academic Press).

87. Pacher, P., Nagayama, T., Mukhopadhyay, P., Bátkai, S., and Kass, D.A. (2008). Measurement of cardiac function using pressure-volume conductance catheter technique in mice and rats. Nat. Protoc. 3, 1422–1434. https://doi.org/10.1038/nprot.2008.138.

88. Varner, K.J., Vasquez, E.C., and Brody, M.J. (1994). Lesions in rostral ventromedial or rostral ventrolateral medulla block neurogenic hypertension. Hypertension 24, 91–96. https://doi.org/10.1161/01.hyp.24.1.91.

89. Wang, X., Liu, Y., Li, X., Zhang, Z., Yang, H., Zhang, Y., Williams, P.R., Alwahab, N.S.A., Kapur, K., Yu, B., et al. (2017). Deconstruction of Corticospinal Circuits for Goal-Directed Motor Skills. Cell 171, 440–455.e14. https://doi.org/10.1016/j.cell.2017.08.014.

90. Selimbeyoglu, A., Kim, C.K., Inoue, M., Lee, S.Y., Hong, A.S.O., Kauvar, I., Ramakrishnan, C., Fenno, L.E., Davidson, T.J., Wright, M., and Deisseroth, K. (2017). Modulation of prefrontal cortex excitation/inhibition balance rescues social behavior in CNTNAP2-deficient mice. Sci. Transl. Med. 9, eaah6733. https://doi.org/10.1126/scitranslmed.aah6733.

91. Flynn, J.R., Brichta, A.M., Galea, M.P., Callister, R.J., and Graham, B.A. (2011). A horizontal slice preparation for examining the functional connectivity of dorsal column fibres in mouse spinal cord. J. Neurosci. Methods 200, 113–120. https://doi.org/10.1016/j.jneumeth.2011.06.017.

STAR★METHODS

KEY RESOURCES TABLE

REAGENT or RESOURCE	SOURCE	IDENTIFIER
Antibodies		
chicken anti-GFP	Aves	GFP-1020; RRID:AB_10000240
rabbit anti-RFP	Abcam	ab34771; RRID:AB_777699
goat anti-cholinergic acetyltransferase (ChAT)	Millipore	AB144P; RRID:AB_2079751
rabbit anti-tyrosine hydroxylase (TH)	Millipore	AB152; RRID:AB_390204
goat anti-5HT	Immunostar	20079; RRID:AB_572262
rabbit anti-c-Fos	Cell Signaling Technology	2250; RRID:AB_2247211
Alexa Fluor 488 donkey anti-chicken	Jackson ImmunoResearch	703-545-155; RRID:AB_2340375
Alexa Fluor 568 donkey anti-rabbit	Thermo Fisher	A10042; RRID:AB_2534017
Alexa Fluor 647 donkey anti-goat	Thermo Fisher	A21447; RRID:AB_2535864
Alexa Fluor 405 donkey anti-rabbit	Abcam	ab175649; RRID:AB_2715515
Bacterial and Virus Strains		
AAV-hSyn-H2B-GFP	This paper	N/A
AAV-CAG-DIO-H2B-GFP	This paper	N/A
AAV-Ef1a-fDIO-H2B-mCherry	This paper	N/A
AAV-hSyn-DIO-ReaChR-Citrine	Lin et al.[76]	Addgene#50955
AAV-Ef1a-DIO-FlpO	Zingg et al.[77]	Addgene#87306
AAV-CAG-fDIO-ChrimsonR-GFP	Klapoetke et al.[78]	Addgene#118295
AAV-Ef1a-fDIO-Cre	Schneeberger et al.[79]	Addgene#121675
AAV-hSyn-fDIO-mGFP-2A-Synaptophysin-mRuby	Beier et al.[80]	Addgene#71761
AAV-DIO-mGFP-2A-Synaptophysin-mRuby	Beier et al.[80]	Addgene#71760
AAV-hSyn-ChR2-EYFP	Karl Deisseroth	Addgene#26973
AAV-Ef1a-fDIO-GCaMP6s	Rylan Larsen	Addgene#105714
AAV-hSyn-DIO-GCaMP6s	Chen et al.[81]	Addgene#100845
AAV-hSyn-fDIO-hM4Di-mCherry	Runegaard et al.[82]	Addgene#154867
AAV-hSyn-DIO-TeLC-EYFP	Fan Wang, MIT	Addgene#135391
AAV-CAG-H2B-tdTomato	Economo et al.[83]	Addgene#116870
Chemicals, Peptides, and Recombinant Proteins		
Pancuronium bromide	Millipore Sigma	P1918
Deschloroclopazine	Tocris	7193
Red Retrobeads IX	LumaFluor Inc.	Red Retrobeads™ IX (100 μl)
NBQX	Tocris	1044
CPP	Tocris	1265
TTX	Tocris	1078
4-AP	Sigma	A78403
BMI	Tocris	2503
Strychnine	Sigma	S0532
4-AP	Tocris	0940
Experimental Models: Organisms/Strains		
Mouse: C57BL/6J	The Jackson Laboratory	Jax#000664
Mouse: Vglut2-ires-Cre	The Jackson Laboratory	Jax#016963
Mouse: Vgat-2A-FlpO	The Jackson Laboratory	Jax#029591

Continued		
REAGENT or RESOURCE	SOURCE	IDENTIFIER
Mouse: ChAT-ires-Cre	The Jackson Laboratory	Jax#006410
Mouse: TH-Cre	The Jackson Laboratory	Jax#008601
Mouse: Ai14	The Jackson Laboratory	Jax#007914
Software and Algorithms		
LabChart	ADInstruments	https://www.adinstruments.com/products/labchart
Doric Neuroscience Studio	Doric	https://neuro.doriclenses.com/products/doric-neuroscience-studio
Notocord-hem	Instem	https://www.instem.com/solutions/notocord/notocord-hem.php
Sirenia Sleep Pro	Pinnacle Technology Inc.	https://www.pinnaclet.com/sleepPRO.html
ZEN Blue	ZEISS	https://www.micro-shop.zeiss.com/en/us/softwarefinder/software-categories/zen-blue/
Fiji ImageJ	Fiji	https://fiji.sc/
QuPath	Bankhead, P. et al.[84]	https://qupath.github.io/
DeepLabCut	Mathis et al.[85]	http://www.mackenziemathislab.org/deeplabcut
MATLAB	MathWorks	https://www.mathworks.com/products/matlab.html
GraphPad Prism	GraphPad	https://www.graphpad.com/
Other		
Millar Mikro-Tip Pressure Catheter	AdInstrument	SPR-1000
Stellar Implantable Transmitter	TSE	Type PBTA-XS-C
PowerLab16/35	ADInstrument	PL3516
Fiber Photometry Console	Doric	FPC

RESOURCE AVAILABILITY

Lead contact
Further information and requests for resources and reagents should be directed to and will be fulfilled by lead contact, Zhigang He (zhigang.he@childrens.harvard.edu).

Materials availability
AAV9retro reported in this study will be available at Addgene.

Data and code availability
- All data necessary to understand and assess the conclusions of this manuscript are presented in the paper and the supplemental information.
- Codes for analyzing neuronal activities and physiological and histological data are available upon request.
- Any additional information required to reanalyze the data reported in this paper is available from the lead contact upon request.

EXPERIMENTAL MODEL AND STUDY PARTICIPANT DETAILS

Mouse Strains
All experimental procedures were performed in compliance with animal protocols approved by the Institutional Animal Care and Use Committee at Boston Children's Hospital. The following mouse lines were used in this study: C57BL/6J wild-type (WT) mouse (Jax#000664), *Vglut2-ires-Cre* (Jax#016963), *Vgat-2A-FlpO* (Jax#029591), *ChAT-ires-Cre* (Jax#006410), *TH-Cre* (Jax#008601), and Ai14 (Jax#007914). Only male mice (P14 to 6 months) were included in this study. For treatment and control groups, mice were used from littermates and the body weight was randomized and assigned to different groups.

METHOD DETAILS

Virus production and injection

All viruses used in this study were produced by Viral Core of Boston Children's Hospital, unless otherwise indicated. The following viruses were used: AAV9retro-hSyn-H2B-GFP, AAV9retro-CAG-DIO-H2B-GFP, AAV9retro-Ef1a-fDIO-H2B-mCherry, AAV9retro-hSyn-DIO-ReaChR-Citrine, AAV9retro-EF1a-DIO-FlpO, AAV8-CAG-fDIO-ChrimsonR-GFP, AAV8-hSyn-DIO-ReaChR-Citrine, AAV9retro-Ef1a-fDIO-Cre, AAV8-hSyn-fDIO-GFP-Synaptophysin-mRuby, AAV8-hSyn-DIO-GFP-Synaptophysin-mRuby, AAV9-CAG-H2B-tdTomato, AAV8-hSyn-ChR2-EYFP, AAV8-Ef1a-fDIO-GCaMP6s, AAV8-hSyn-fDIO-GFP, AAV8-hSyn-DIO-GCaMP6s, AAV8-hSyn-fDIO-hM4Di-mCherry, and AAV8-hSyn-DIO-TeLC-EYFP. The titers of the viruses were adjusted to $0.5{\sim}2e+13$ gc/ml for injection.

For spinal cord injection at P14, mice were anesthetized, shaved, and positioned in the ultrasound injection platform with heated base set at $37^{\circ}C$.[28] A glass pipette was guided by the ultrasound probe (MS550, Ultrasonic Vevo 3100) and inserted into the spinal cord. For the most rostral injection site in the cervical spinal cord, the position was located 1.5mm caudal to C1 vertebrate to avoid virus diffusion to brainstem. Injections were made bilaterally with two different depths targeting lamina 1-5 and lamina 6-9 of gray matter. Injections were made at the gap between every two vertebrae, corresponding to spinal segment C3 to L6. A total volume of 1.8 µl was injected in cervical (C3-C8) and lumbar (L1-L6) spinal cord, and 2.4 µl in the thoracic (T1-T13) spinal cord.

For the spinal cord injection of retrobeads in adult mice (P56), mice were positioned on the stereotaxic frame, with spinal vertebrate secured using spinal clamp accessories. A laminectomy was made at the cervical (C4-6) and lumbar (L2-4) spinal cord, and a total volume of 2.4 µl virus was injected in bilateral grey matter at 1mm and 0.6mm depths, 0.35mm lateral to midline, in each part of spinal cord. For the spinal cord injection aiming to limit the virus diffusion so as not to reach spinal levels containing SPGNs, a laminectomy was performed at the T13 vertebra, and a total volume of $50{\sim}100$ nl of virus was injected into the L4/5 spinal cord segments at 1mm and 0.6mm depths, 0.35mm lateral to midline. The samples were verified with post hoc histology and only animals with no viral diffusion to SPGNs at the L2 spinal cord were included in further analysis.

For brainstem injections, mice were positioned on a stereotaxic frame. A craniotomy was made on the skull on top of the cerebellum, and a glass pipette was inserted perpendicularly into target brainstem regions according to mouse brain atlas.[86] The coordinates for different brainstem targets are as follows (zero from Bregma; AP, anterior-posterior; ML, medial-lateral; DV, dorsal-ventral from dura; in mm): GiA, AP-6.1, ML0.3, DV-4.9; GiV, AP-6.7, ML0.3, DV4.9; MdV, AP-7.3, ML0.3, DV4.9; rVLM, AP-7.0, ML1.2, DV4.9. A volume of 0.2 µl was injected at each coordinate. In the loss-of-function experiment with viral expression of hM4Di or TeLC, the following injection coordinates were used: rVMM, AP-5.8/-6.1/-6.4, ML±0.3, DV-5.0/-4.7. A volume of 0.2 µl was injected at each coordinate.

Opto-stimulation, EMG and blood pressure recording in anesthetized mice

Mice were anesthetized with ketamine/xylazine (100/10 mg/kg, i.p.) and body temperature was maintained at $37^{\circ}C$ with controlled heat pad (HB101/2; Panlab). The trachea was cannulated with a customized trachea tube with Luer connector. The procedure for measuring blood pressure from the left carotid artery is similar to what had been described before.[87] In brief, the left sternohyoid muscle next to trachea was separated to expose the left common carotid artery. The cranial end (proximal to the internal and external carotid artery bifurcation) was ligated with suture. A vessel clamp was placed on the caudal end temporarily. An arteriotomy was created with a modified 26-gauge needle and a pressure catheter (SPR-1000, 1F; Millar; calibrated with pressure gauge each time before use) was introduced to the left carotid artery and advanced to aortic arch. The blood pressure wave form was monitored in real time to ensure accurate placement. The catheter was secured in place with double suture. Customized EMG electrodes were connected to longissimus thoracis (upper trunk muscle) on the right side of body. Blood pressure was amplified with Bridge Amp (ADInstruments). EMG signals were filtered at 0.1-1000 Hz and amplified 1000x using a differential AC amplifier (Model 1700; A-M Systems). Both blood pressure and EMG signals were digitized at 4000Hz with Power Lab 16/35 and processed in LabChart 8 (ADInstruments). Mean arterial pressure (MAP) was measured from each cardiac cycle by cyclic measurement.[21,36,88] Heart rate was extracted from blood pressure signal using cyclic measurement. To measure the EMG and blood pressure response, mice were maintained anesthetized with supplemental ketamine/xylazine (1/3 of initial dose every 1 hour). To assess the blood pressure without the interference of muscle contraction, pancuronium bromide (1mg/kg, i.p.; Tocris) was administered to paralyze muscles (with supplemental dose of 0.5mg/kg every 1 hour), and a ventilator (SAR-830/P; CWE Inc.) was connected to the trachea tubing. 95% O_2 and 5% CO_2 were supplied at breathing rate of 150bpm, end-inspiratory pressure of $12cmH_2O$, and 40% of inspiratory time each cycle. To verify the effectiveness of the pancuronium, EMG activities were monitored during and after the application of pancuronium to confirm the complete absence of EMG activities.

To test the minimum stimulation threshold and fine tune the spatial resolution, mice were anesthetized and paralyzed with muscle relaxant. An optical fiber (200um, 0.39NA, RWD) was dipped with fluorescent dye to label insertion track, inserted perpendicular from the cerebellum targeting the GiA (AP-6.1, ML0.2, in mm). 473nm laser stimulation (1.0mW, 5ms pulse, 20Hz, 500 pulse train) was applied. The optical fiber was lowered down with 0.5mm steps in depth. Once a blood pressure response was observed, the laser intensity was lowered to threshold. This procedure was repeated until a minimum threshold was identified at a hotspot depth. The fiber tip was finally lowered down to the bottom where no response was expected, to confirm the laser was restricted at the fiber tip, as well as to confirm the depth of the hotspot. To test minimum stimulation threshold for EMG response, the experiment was carried

out in a separate preparation without muscle relaxant, and a similar procedure was performed to guide the optical fiber to the same hotspot (AP-6.1, ML0.2, DV-4.5, in mm). Laser stimulation (5 ms pulse, 20 Hz, 10 pulse train) was applied and repeated 5 times at intensity of 0.002mW and up, until an EMG response was observed. Since the measured stimulation threshold of an EMG response was lower or similar to that of blood pressure response, the same stimulation intensity was used in an individual subject to cover the same area in the brain wide mapping experiment.

To map the EMG, blood pressure, and heart rate response brain wide, the following coordinates were used where SPNs were identified (zero from Bregma; AP, anterior-posterior from Bregma; ML, medial-lateral from Bregma; DV, dorsal-ventral from dura; in mm): M1S1, AP 0, ML 1.0, DV 0.6; PVN, AP -1.3, ML 0.3, DV -4.5; LH, AP -1.9, ML 0.8, DV -4.5; RN, AP -3.7, ML 0.75, DV -3.5; MRN, AP -3.7, ML 0.75, DV -2.5; PPN, AP -4.6, ML 1.2, DV -2.5; PnO, AP -4.5, ML 1.2, DV -4.0; LDTg, AP -5.2, ML 0.7, DV -2.5; SubC, AP-5.5, ML 0.7, DV -2.5; PnC, AP -5.2, ML 0.7, DV -4.0; Ve, AP -6.3, ML 0.9, DV -3.0; CB, AP -6.4, ML 0.9, DV -2.0; GiA, AP -6.2, ML 0.2, DV -4.5; GiV, AP -6.7, ML 0.2, DV -4.5; MdV, AP -7.2, ML 0.2, DV -4.5; LPGi, AP -6.9, ML 1.1, DV -5.0; NTS, AP -7.7, ML 0.5, DV -2.5. Laser stimulation (0.04 ~ 0.23 mW, 5 ms pulse, 20Hz, 500 pulse train) was applied and repeated 3 times at each site. The fiber-optic tip was dipped with dye at each insertion to label the insertion track and tip location. Fiber tip locations were examined in coronal brain sections and the actual coordinates were subjected to adjustment and registered in brain atlas. The experiment was performed first with ketamine/xylazine only. After that, mice were paralyzed with pancuronium administration, and stimulations were applied to the same regions to test the blood pressure response only.

EMGs were analyzed similar to what has been described before.[89] Briefly, EMG signals were high-pass-filtered at 10Hz, rectified to a positive value, and averaged every 0.5s. Then EMGs were averaged from repeated trials and normalized to the maximum response amplitude among all brain regions. MAP was measured from each cardiac cycle. Heart rate was extracted from the cyclic measurement of blood pressure. Blood pressure and heart rate response were calculated by subtracting the pre-stimulation baseline level from the maximum amplitude during stimulation and averaged across repeated trials.

To stimulate the SPN projections in the spinal cord, the spinal cord was exposed with dorsal muscles removed, and fixed on the stereotaxic frame with spinal clamp. The fiber-optic tip was guided to the vertebrate gap of the C4, T3, T9 or L4 in the spinal cord, and a 593nm laser (3 mW, 5ms pulse, 20Hz, 500-pulse train) was delivered. 593nm laser was used instead of 473nm laser because of the better tissue penetration of red-shifted laser to activate down to the ventral spinal cord. After stimulation in the intact spinal cord, a full transverse transection was made at C4 spinal cord using a fine feather blade, and bleeding was stopped before proceeding to stimulation and recording after transection.

Chronic recording of autonomic, EEG and EMG in behaving mice

The procedure for implanting a telemetry device for chronic recording of blood pressure and heart rate has been described before.[56] In brief, mice were anesthetized with ketamine/xylazine. Incisions were made on the dorsal and ventral neck. A telemetry device with a pressure catheter (Type PBTA-XS-C; TSE) was placed in the dorsal pocket on the back. The pressure catheter was routed ventrally and placed in the left carotid artery, with a similar procedure described earlier in the acute blood pressure recording. Catheter wire was secured with suture to the surrounding musculature. After surgery, mice were allowed to recover for 5-7 days before behavioral assessment and recording. Blood pressure was recorded at 250Hz using Stellar Telemetry System (TSE) and processed using Notocord software (Instem). Data was then synchronized with other recording data using LabChart 8. MAP and heart rate were extracted from the original blood pressure signal using cyclic measurement function in LabChart. For each animal, the pressure catheter was calibrated using a sphygmomanometer before implantation, and a final measurement was performed after subject was euthanized to detect any baseline drift during implantation. Baseline drift was adjusted by dividing the final drift value to the days implanted and applied to the day when recording was performed.

To record EEG and EMG in behaving mice, mice were anesthetized with ketamine/xylazine. An incision was made on the scalp. The customized EEG electrodes were secured with bone screws on the left and right skull on top of the parietal cortices (AP-1.0, ML1.5), and the reference electrode was secured with bone screw on the skull on top of the cerebellum. Differential EMG electrodes were placed in the neck muscle (trapezius muscle, cervical part). The EEG/EMG electrode socket was secure on the skull with dental cement. After surgery, mice were allowed to recover for 5-7 days before behavioral assessment and recording. EEG and EMG signals were amplified 1000x, filtered at 0.1~1000 Hz (1700; A-M System), sampled at 2000 Hz using PowerLab 16/35 (ADInstrument). In 24-hr recording in sound-proof chamber, EEG and EMG signals were amplified 100x (8202-SL; Pinacle), filtered at 0.5~500 Hz, and sampled at 1000 Hz using Sirenia Sleep (Pinnacle). Data was transformed and analyzed with LabChart 8 (ADInstrument). Video tapes were recorded simultaneously at 10-30fps, and the head position was tracked with a deep learning algorithm (DeepLabCut) to calculate movement speed. For EEG analysis, the power spectrum, and the percentage of total power for delta (1-4 Hz) and theta (5-9 Hz) frequency bands was calculated by Multitaper spectral analysis.[52] EMG signal was highpass filtered at 10Hz, rectified to positive value, averaged every 1 second, and normalized to proper reference value (mean EMG amplitude of pre-treatment baseline in Figures 6 and S6; mean EMG amplitude of entire recording period in Figures 7, S5, and S7). In some cases when ECG artifact was presented in EMG recording, a customized algorithm was applied to detect ECG event and the values were zeroed within event window of 10 ms. For sleep scoring, four stages were scored based on the following criteria: 1) Active: high EMG tone with burst (or high movement (>1 cm/s) in loss-of-function assay, same applied to following conditions), low delta (<30%), low theta (<40%); 2) Quiet: high EMG tone without burst (or low movement (<1 cm/s)), low delta (<30%), low theta (<40%); 3) NREM sleep: low EMG tone (or low movement (<1 cm/s)), high delta (>30%), low theta (<40%); 4) REM sleep: low EMG tone (low movement (<1 cm/s)), low delta (<30%),

high theta (>40%). The threshold of delta and theta bands were subjected to 5% adjustment based on individual variation and verified by different experimenters.

Fiber photometry recording on rVMM SPNs

To selectively label SPNs in rVMM, 1) AAV9retro-EF1a-DIO-FlpO were injected into spinal cord of P14 *Vglut2-Cre* mice, or 2) AAV9retro-EF1a-fDIO-Cre into P14 *Vgat-FlpO* mice. At the adult stage, 1) AAV8-Syn-fDIO-GCaMP6s or 2) AAV8-Syn-fDIO-GFP was injected into rVMM (AP -6.0 ~ -6.5, ML 0.2, DV -4.8) of *Vglut2-Cre* mice or 3) AAV8-Syn-DIO-GCaMP6s into rVMM of *Vgat-FlpO* mice. One week after the virus injection, EEG electrodes, a reference electrode and EMG electrodes were placed as mentioned above. The optical fiber was implanted ~ 300 nm above the viral injection site to target SPNs with concurrent monitoring of the photometry signal. All implants were secured with dental cement. After all behavioral experiments, histology verification was conducted to exclude animals with mistargeted viral expression and optic fiber locations for analysis.

After at least one week of recovery, EEG/EMG and photometry signals, together with behavioral videos, were recorded from the mice in a home cage condition (open arena with home cage bedding) or on a treadmill apparatus. In brief, EEG and EMG signals were amplified and filtered (0.1-1000 Hz) by A-M systems, then digitalized with Power Lab 16/35 (ADInstrument). A synchronizing signal was generated by Doric Neuroscience Studio and fed into Power Lab to synchronize photometry, video, and EEG/EMG recordings.

ECG artifact in EMG trace was detected by LabChart cyclic measurement function and removed offline as mentioned above. Then the cleaned EMG signal was rectified and smoothed with 1 second window. EEG and rectified EMG were exported to MATLAB for synchronization with photometry data and spectrum analysis. EEG spectrograms were computed using the Multitaper method[52,53] with the following parameters: 5-second window length, 1-second step size, time-half-bandwidth product of 2.5, and 4 Slepian tapers, which provides a 1 Hz spectral resolution. EEG band power density (delta: 1-4 Hz; theta: 5-9 Hz) was computed by integrating the power in the corresponding frequency range and divided by the total power from 1 to 20 Hz. Z-scored EMG data was first downsampled to the photometry (dFF) resolution, then a 5-second moving average smoothing window was applied to both z-scored dFF (z-dFF) and downsampled EMG. After that, Pearson correlation coefficients were calculated to evaluate the correlations between z-dFF with other parameters. To verify the time-locked correlation, EMG, EEG delta-band %, or EEG theta-band % were randomized along the time domain, and Pearson correlation analysis was performed again with z-dFF. Neutral correlation was observed (data not shown), further validating the correlation shown in Figures 5 and S5. To compare the Pearson's correlation coefficient, the coefficients were transformed into normal distributions using Fisher's transformation $z = arctanh(r)$ and then compared using appropriate statistical tests.

Animal behavioral state was segmented into four according to the corresponding signature EEG and EMG features: Active (high EMG with burst firing and desynchronized EEG), Quiet (high EMG tone with few or no burst firing and desynchronized EEG), NREM (low EMG tone with high EEG delta-band power density (>30%)), and REM (low EMG tone with high EEG theta-band power density (>40%) and low delta-band power density (<30%)).

Photometry signals from 405nm (isosbestic signal) and 465nm (calcium dependent signal) and behavioral video (30 fps) were captured with Doric Neuroscience Studio at 120Hz. Photometry data was exported to MATLAB. dFF was calculated $dFF = (F-F0)/F0$, where F0 is the fitted isosbestic signal and *F* is the calcium dependent signal.[90] Z-scored dFF (z-dFF) was used for synchronization and further analysis. For open arena recording, z-dFF episodes of the same behavioral state were pooled together. For state transitions, z-dFF of 9 seconds before and after transition onset are pooled together. For treadmill running, locomotion speed of the animals was tracked by DeepLabCut.[85] Z-dFF of 2 seconds before and 2 seconds after, or 30 seconds before and 30 seconds after treadmill onset of each speed were pooled to generate averaged traces and the group comparison. The time windows when mice were quiet during treadmill OFF stage were the baseline of 0 cm/s to avoid confusion with spontaneous movement and locomotion. A continuous quiet window larger than 30 seconds from each mouse was pooled to compute the average trace in Figure 5J, and the average z-dFF of all quiet windows was used for group comparison in Figure 5L. To show the dFF changes during transition of locomotion status, 2 seconds around the treadmill onset of each speed are pooled together in Figure 5K. For running disk recording, mice movement were tracked with DLC, and the speed was calculated. Correlation of the calcium activity and running speed were computed after 5 seconds smoothing and down-sampling to 1Hz.

Behavioral tests

24-hour sleep recording was performed on a 12-hour dark-light cycle (7pm-7am dark, 7am-7pm light). Mice were placed in the sound-proof chamber with normal bedding, food and water. EEG/EMG signals and video tape were collected with Sirenia Sleep software (Pinnacle Technology Inc.). Blood pressure signals were collected simultaneously with Stellar Telemetry System (TSE) and Notocord Software (Instem).

The open arena test was performed in a square arena (30x30cm) between 10am-2pm. Before the test, mice stayed in their home cage in the test room for 30 minutes. The mice were then placed in the open arena for 10 minutes, while EMGs, autonomic readouts and video tape were recorded simultaneously. In the case that the test was repeated for different treatments, the repeat test was performed 3-7 days after the previous test to avoid adaptation to the environment.

For the treadmill running test, a treadmill with programmable speed control was used (Exer 3/6; Columbus Instruments). Mice were allowed to acclimate the treadmill at 5 cm/s for 5 minutes one day before the test. During the test, mice were placed on the treadmill for 5-10 minutes at 0cm/s as baseline, where autonomic readouts and EMG were recorded. The period when mice were quiet was

considered baseline of 0cm/s to avoid confusion with spontaneous locomotion. The treadmill was then turned on at 10, 20, 30 cm/s, 1 minute for each speed with 1 second acceleration between speeds. When the mouse's body was dragged against the back wall of the treadmill for more than consecutive 5 seconds, it was considered as not being able to keep up on treadmill and the treadmill was manually stopped. The body position in the treadmill was recorded with a top-down camera at 30fps or a side-view camera at 120fps. Three test sessions were performed with 5-minute intervals between sessions. An average of three sessions was calculated for individual subjects. To compare the blood pressure and EMG levels during treadmill running between silenced and control groups, the duration of running in control groups was subsampled as the mean duration of running in the silenced groups at each speed, and 30cm/s was omitted from comparison as most silenced mice were not able to run.

To silence excitatory SPNs, hM4Di was allowed to be expressed for 3 weeks after virus injection. DCZ (1mg/kg, i.p., dissolved in 2% DMSO in saline) or vehicle (2% DMSO in saline) was injected, and behavioral tests were performed 10-180 minutes after injection. For permanent silencing of inhibitory SPNs, TeLC was allowed to be expressed for 3 weeks after virus injection before behavioral tests.

For the horizontal running disc assay, an exercise saucer (You & Me; Petco) was placed in the mouse housing chamber to allow them to run voluntarily on the saucer. To allow the mice to acclimate the saucer, a small size saucer (12.7 cm in diameter) was placed in the housing chamber for 3 days. During the testing session, a medium size saucer (19.05 cm in diameter) was placed in the recording chamber, and the saucer rotation and mouse activity was video-taped at 30 fps through a top-down camera. Three markers were drawn on the edge of the saucer. The markers and mouse body mass locations in each frame were tracked with DeepLabCut to calculate the mouse locomotion speed.

Slice recording on sympathetic preganglionic neurons in thoracic spinal cord

To express channelrhodopsin (ChR) in rVMM neurons, AAV8-Syn-ChR2-EYFP was injected in rVMM of *ChAT-Cre: tdTomato* reporter mice at P4. In brief, neonatal pups at P4 were anesthetized with ice and placed under the ultrasound probe (MS550, Ultrasonic Vevo 3100). A glass pipette was guided to the midline of rVMM and 0.8ul of AAV8-Syn-ChR2-EYFP virus was injected at 0.1ul/min. Pups were then placed on heat pad to recover and returned to normal feeding.

After 4-6 weeks (postnatal day 33-46), the spinal cord was removed by hydraulic extrusion with cold slicing solution. Slicing solution composition was (in mM): NaCl 80, Sucrose 75, NaH$_2$PO4 1.25, NaHCO$_3$ 26, CaCl$_2$ 0.5, MgCl$_2$ 3.5, D-glucose 10, Na-ascorbate 1.3, Na-pyruvate 3, myo-Inositol 3. The thoracic cord was mounted on agarose block with the ventral part facing the glue. The agarose block was glued to the chamber filled with ice-cold slicing solution. Horizontal slices (200 μm) were cut in a similar way to a previous method.[91] The blade approached in a perpendicular direction to the long axis of tissue with vibrating slicer (VT1200S, Leica). The second and third slices from the dorsal surface were further cut into about 4 pieces per slice manually. Tissues were incubated in ACSF for 60 min at 35-36 °C, then kept in room temperature for at least 1 hour (23-24 °C). ACSF solution consists of (in mM): NaCl 120, KCl 2.5, NaH$_2$PO$_4$ 1.25, D-Glucose 20, NaHCO$_3$ 26, CaCl$_2$ 2, MgCl$_2$ 1, Na-ascorbate 1.3, Na-pyruvate 3, myo-Inositol 3.

Tissue was transferred to the recording chamber maintained at 31-32 °C (BX50WI, Olympus). ACSF flowed 2-3 ml/min. IML region was identified with tdTomato fluorescence (550 nm LED, pE-4000, CoolLED). Whole cell recording was obtained with pipettes (2-4 MΩ, BF150-86-10, Sutter). Pipette solutions for EPSC experiment contained (in mM) K-gluconate 130, KCl 5, MgATP 4.0, NaGTP 0.5, phospho-creatine 10, HEPES 10, EGTA 0.5. pH adjusted to 7.2-7.4 with KOH, osmolality 290-300 mOsm. Pipette solution for IPSC experiment contained (in mM) CsMeSO$_3$ 120, CsCl, HEPES 10, EGTA 0.5, MgATP 4.0, NaGTP 0.5, phospho-creatine 10, TEA-acetate 10, QX314-Br 2.5. pH adjusted to 7.20 with CsOH (50%). Osmolality was 290-300 mOsm. Green fluorescent dye was added to the pipette solution to mark the recorded cell (20 μM, A10436, Invitrogen).

In voltage-clamp, the holding potential was -70 mV for EPSC or +20 mV for IPSC experiment. To activate ChR synaptic projection from brainstem to the recorded cells, LED 470 nm (11.08 mWatt, PM100D, ThorLAB) was applied through a 60x objective (0.90 NA, Olympus). A single pulse (5 ms, 0.1 Hz) continued for ~10 min in ACSF before drug applications. For EPSC, TTX (0.5 μM), 4-AP (200 μM), NBQX (5 μM), and CPP (10μM) were sequentially added. For IPSC experiment, TTX, NBQX, CPP, 4-AP, Strychnine (1.0 - 1.3 μM), and BMI (10-13 μM) were sequentially applied. After NBQX + CPP or Strychnine + BMI condition, series resistance (<35 MΩ) was measured with Membrane Test in pClamp. Recording continued in ACSF with 4-AP for at least 20 min to check cell viability. The measured liquid junction potential was small, -5 mV, and therefore was not corrected. Drug and chemicals were purchased from Tocris and Sigma.

Data were acquired with Multiclamp 700B (Molecular Device), filtered (low-pass 3 KHz, Bessel filter), and sampled at 10 or 20 KHz (pClamp 10). For signal analysis (Clampfit or MATLAB), five traces were averaged in each condition. For EPSC or IPSC amplitude, inward or outward peaks within a 20 ms window from the onset of light stimulation were detected.

After spinal slice recording, viral expression in brainstem was examined with 100μm brain sections made from the vibratome and only those with expression restricted in rVMM were included in final analysis.

Normality was tested with Shapiro-Wilk test. Non-normal data was expressed with median and range. For repeated events, repeated nonparametric ANOVA (Friedman test with Dunn's post hoc test) was applied.

Immunohistochemistry

At the end of the experiment, mice were anesthetized with ketamine/xylazine, and perfused transcardially with 1X phosphate-buffered saline (PBS) followed by 4% paraformaldehyde. The tissue was post-fixed with 4% paraformaldehyde at 4°C overnight. Brain

and spinal cord tissue were dissected and dehydrated in 30% sucrose in 1X PBS. The tissues were sectioned using a cryostat (50μm for brain, 30μm for spinal cord). Sections were rinsed with 0.5% Triton-100 in PBS 5 minutes for 2 times and then treated with blocking solution containing 10% normal donkey serum and 0.5% Triton-100 in PBS for 2 hours at room temperature. Sections were then incubated with primary antibodies overnight at 4C, washed 0.5% Triton-100 in PBS for 3 times, and incubated with secondary antibodies for 2 hours at room temperature. After thoroughly washed with PBS 3 times, sections were mounted with mounting medium with or without DAPI for imaging and storage. The following antibodies were used at dilution of 1:500 if not otherwise specified: chicken anti-GFP (GFP-1020, Aves), rabbit anti-RFP (ab34771, Abcam), goat anti-cholinergic acetyltransferase (ChAT) (1:200; AB144P, Millipore), rabbit anti-tyrosine hydroxylase (TH) (AB152, Millipore), goat anti-5-HT (20079, Immunostar), rabbit anti-c-Fos (2250; Cell Signaling Technology), Alexa Fluor 488-conjugated donkey anti-chicken (703-545-155, Jackson ImmunoResearch), Alexa Fluor 568-conjugated donkey anti rabbit (A10042, Thermo Fisher), Alexa Fluor 647-conjugated donkey anti goat (A21447, Thermo Fisher), and Alexa Fluor 405-conjugated donkey anti rabbit (ab175649, Abcam).

Imaging and histological analysis

Images were taken using the following microscope and objectives: Zeiss LSM 900 Confocal Laser Scanning Microscope, wide field, 10x objective (Figures 1A, 1E, 1J, 2B, S1D, S1L, S2G, S6A–S6C, and S7A–S7C); wide field, 5x objective (Figures S4F–S4H), 10x objective (Figure 5B); LSM 900, laser scanning, 10x objective, z-stack of 5 μm (Figures 2C, S1C, S1E–S1G, S2B, S2H, S3I, S3L, and S3M); LSM 900 or LSM 980 Confocal Microscope with Airyscan 2, laser scanning, 20x objective, z-stack of 1 μm (Figures 4, S2C, S1D, and S3). TissueCyte Serial Two-Photon Tomography (FigureS1B).

For 3D reconstruction of whole brain SPNs, the brains with retrograde virus labeling were processed and imaged with the TissueCyte serial two-photon tomography platform. Images of 25 μm thickness were stacked with MicroFile+ (MBF Bioscience). The stacked image was then imported into Neuroinfo (MBF Bioscience) for H2B signal detection, and their locations were then registered to the Allen Mouse Common Coordinate Framework (Allen CFF). The detected H2B signals were manually assigned with different colors according to the previous registration. Videos and horizontal, coronal projections of the reconstructions were obtained from Neuroinfo's 3D visualization module.

The contour map for fiber density was plotted by first loading the images into MATLAB and subtracting the background. Then the images were binarized with a threshold of 80 and bright dots with less than two connected pixels were considered as noise and were removed. The image was separated into 16-by-16 equally spaced bins and the number of bright dots that fell in each bin were counted. To make the contours more natural and less rigid, the count results were smoothed with 100-by-100 bins. Contour plots were generated from the smoothed results.

To examine the innervations of SPNs in spinal cord and brain regions, synaptophysin-RFP signals were captured together with green fluorescence of the fibers. Spinal cord and brain regions found to contain fibers were also checked for synaptophysin-RFP signals co-expressing in the fibers to confirm that they are innervated with synaptic boutons. Synaptophysin-RFP channels were not overlaid in Figures 4C, 4E, 4F, and S3 because of the smaller size and weaker fluorescence that are not visible in the larger scale images.

To examine the colocalization of synaptic boutons on ChAT$^+$ IML neurons in thoracic cord, images were captured with a 20x objective at 1 μm z-stack interval. Images were examined in orthogonal projection mode in which the candidate colocalized synaptic boutons were also visualized at z-stack of their own x and y position. Only those boutons also found colocalized with ChAT$^+$ cell bodies or dendrites at z-stack of their own x and y position were counted as colocalization.

To analyze the rostral-caudal distribution of labeled cells, 50 μm serial coronal brain sections were obtained, and analysis (including cell counting) was performed on every 3rd section if not otherwise specified. Cell detection and counting was performed using QuPath.[84]

QUANTIFICATION AND STATISTICAL ANALYSIS

Statistical analysis was performed using GraphPad Prism 9. Shapiro-Wilk tests were performed to check if data set is normally distributed. Subsequent parametric tests were performed on normally distributed data sets, and non-parametric tests were performed on non-normally distributed data set. Paired or unpaired t tests were performed for single comparison between two groups depending on experimental design. One-way, two-way ANOVA, or mixed-effects analysis were performed on comparisons between three or more groups depending on experimental design. Post hoc multiple comparisons were carried out with appropriate corrections. Differences were considered statistically significant if p value was below 0.05.

Supplemental figures
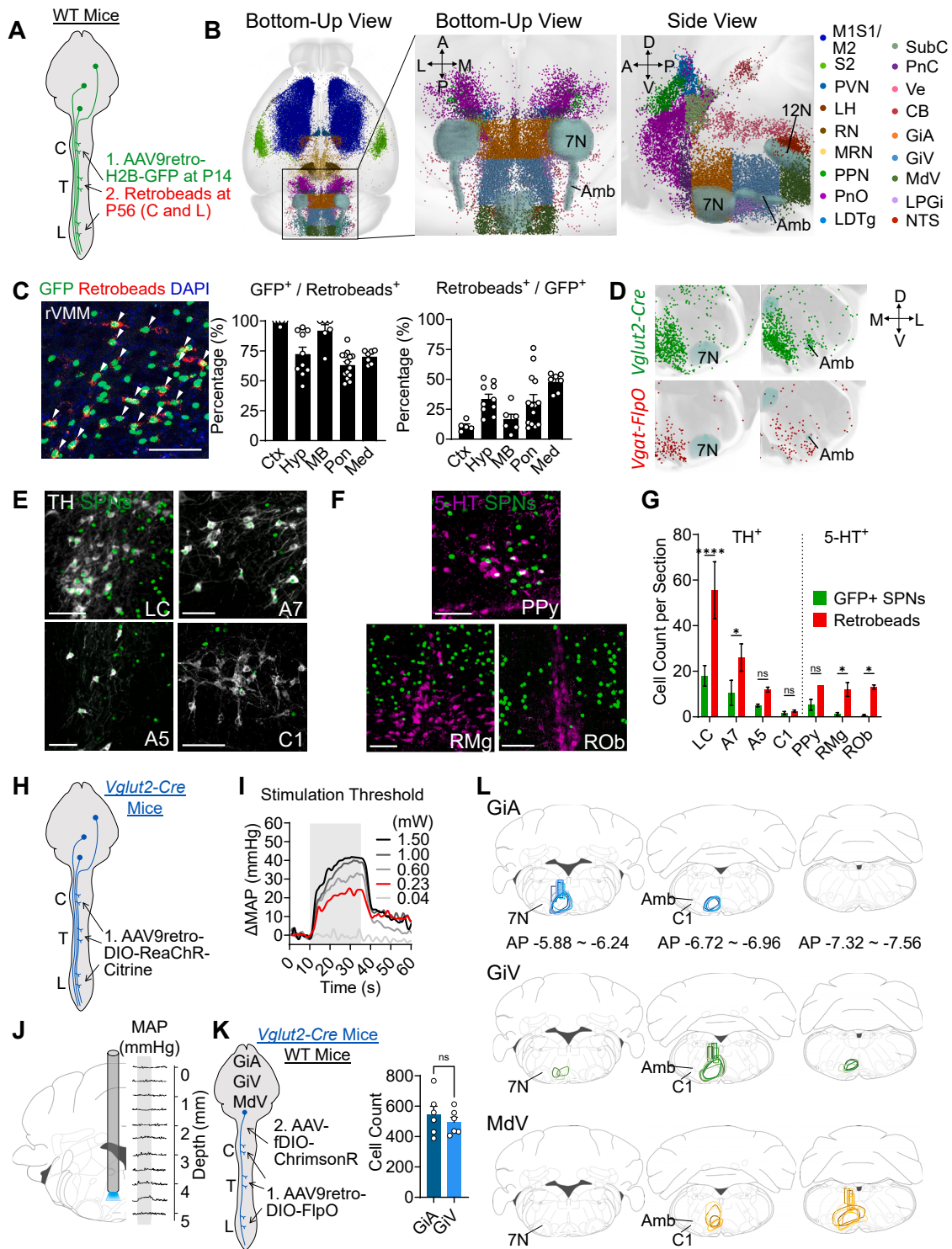
Figure S1. Anatomical characterization of SPNs, related to Figure 1

(A) Strategy of retrograde labeling of SPNs with AAVs and retrobeads in wild-type (WT) mice.

(B) 3D reconstruction showing AAV-labeled SPN somas (marked by dots) from serial horizontal section and imaging of whole brain (left) and zoom-in views of pons and medulla (middle and right). Landmarks (7N, facial nucleus; Amb, ambiguus nucleus; 12N, hypoglossal nucleus) were also indicated in the middle and right panels.

(C) Colocalization of GFP-labeled SPNs in retrobead-labeled population and vice versa. Scale bar, 100 μm. Quantification: mean ± SEM, on multiple coronal sections from 3 mice. Ctx, cortex; Hyp, hypothalamus; MB, midbrain; Pon, pons; Med, medulla.

(D) 3D reconstruction of medulla showing the distribution of excitatory and inhibitory SPNs, labeled by AAV9retro-DIO-H2B-GFP or AAV9retro-fDIO-H2B-mCherry injection in the spinal cord of *Vglut2-Cre* or *Vgat-FlpO* mice, respectively.

(E and F) Colocalization of SPNs (AAV labeled) and TH⁺ (E) or 5-HT⁺ cells (F) (immunostaining). Scale bar, 100 μm. LC, locus coeruleus; A7/A5, noradrenergic neuron groups 7 and 5 in pons; C1, adrenergic neuron group in ventrolateral medulla; PPy, para-pyramidal nucleus; RMg, raphe magnus nucleus; ROb, raphe obscurus nucleus.

(G) Cell counts of TH⁺ or 5-HT⁺ SPNs labeled by AAV versus those labeled by retrobeads ($n = 2$ to 4 sections from 2 brain samples). *, $p < 0.05$; ****, $p < 0.0001$; ns, not significant; unpaired t test.

(H) Strategy of ReaChR-assisted retrograde labeling of excitatory SPNs for mapping somatomotor and sympathetic response upon opto-stimulation.

(I) Examples of blood pressure change at GiA in response to different laser intensity, determining the threshold for brain-wide mapping.

(J) Example of blood pressure change upon opto-stimulation (gray shade) at different depths (with 0.5 mm step) from dura of cerebellum to bottom of medulla. Blood pressure response only occurred in 4.5 mm depth, but not other depths.

(K) Strategy of intersectional labeling of excitatory SPNs with ChrimsonR in GiA, GiV, or MdV. WT mice were injected as control. Cell counts (mean ± SEM) from ChrimsonR-labeled excitatory SPNs in GiA and GiV (1/3 of all coronal brain sections). ns, not significant; unpaired t test.

(L) Viral expression area for intersectional labeling of ChrimsonR targeting GiA (blue), GiV (green), and MdV (yellow) nuclei. Graded colors marked individual subject. Rectangle shapes: location of fiber-optic tip for individual subject.
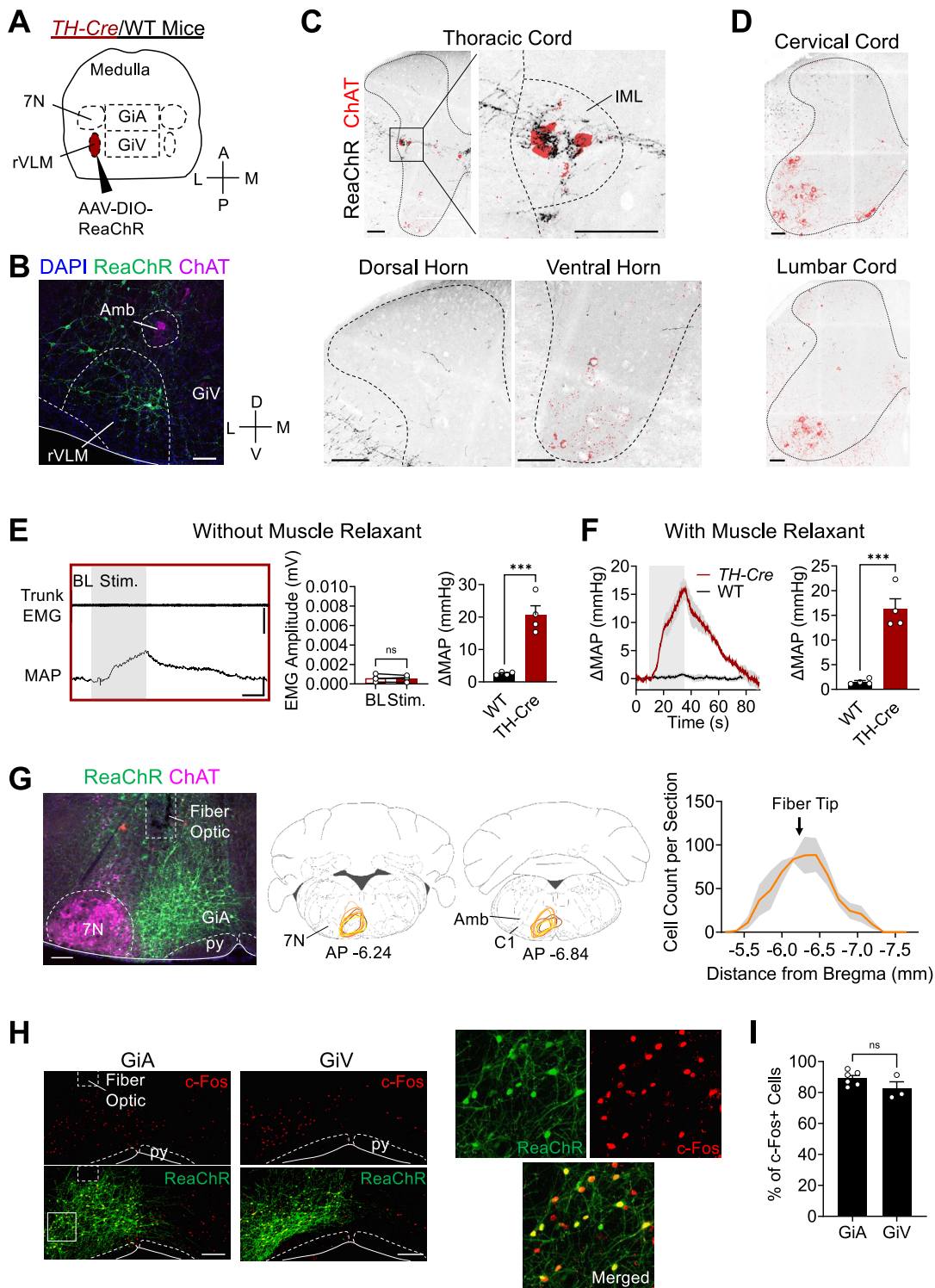
Figure S2. C1 neurons are anatomically and functionally distinct from excitatory rVMM SPNs, related to Figure 2

(A) Injection location and strategy of labeling C1 neurons with ReaChR. R, rostral; C, caudal; L, lateral; M, medial.

(B) Representative image showing C1 neurons labeled with ReaChR located lateral to GiV, with reference to ambiguus nucleus (Amb) as anatomical landmark. D, dorsal; V, ventral.

(C and D) Spinal innervation of C1 neurons in thoracic (C), cervical, and lumbar spinal cord (D), with zoom-in images in IML, dorsal horn, and ventral horn of thoracic spinal cord. Scale bar, 100 μm.

(E) Left: time course of EMG and MAP changes upon opto-stimulation of C1 neurons (gray shade), under the condition of no muscle relaxant. Middle: EMG level at baseline (BL, 10 s prior to stimulation onset) and during stimulation (Stim.). ns, not significant; paired t test. Right: maximal changes of MAP upon stimulation (mean ± SEM). ***, $p < 0.001$; unpaired t test.

(F) Time course (left) and maximal changes of MAP (right) upon opto-stimulation under the presence of muscle relaxant (mean ± SEM). ***, $p < 0.001$; unpaired t test.

(G) Left: location of fiber-optic tip and inhibitory SPNs labeled with ReaChR in coronal brain section. Scale bar, 200 μm. Middle: ReaChR expression areas in coronal levels. Right: cell distribution along rostral-caudal axis (mean ± SEM).

(H) Left: colocalization of c-Fos-expressing nuclei and ReaChR-labeled inhibitory SPNs shown in coronal brain sections. Scale bar, 200 μm. Right: enlarged image (from white square region in left panel) shows colocalization of c-Fos and ReaChR-labeled SPNs in split and merge channels.

(I) Percentage of c-Fos⁺ cells in GFP⁺ SPNs (mean ± SEM, cell counts from multiple sections of 2 brain samples).
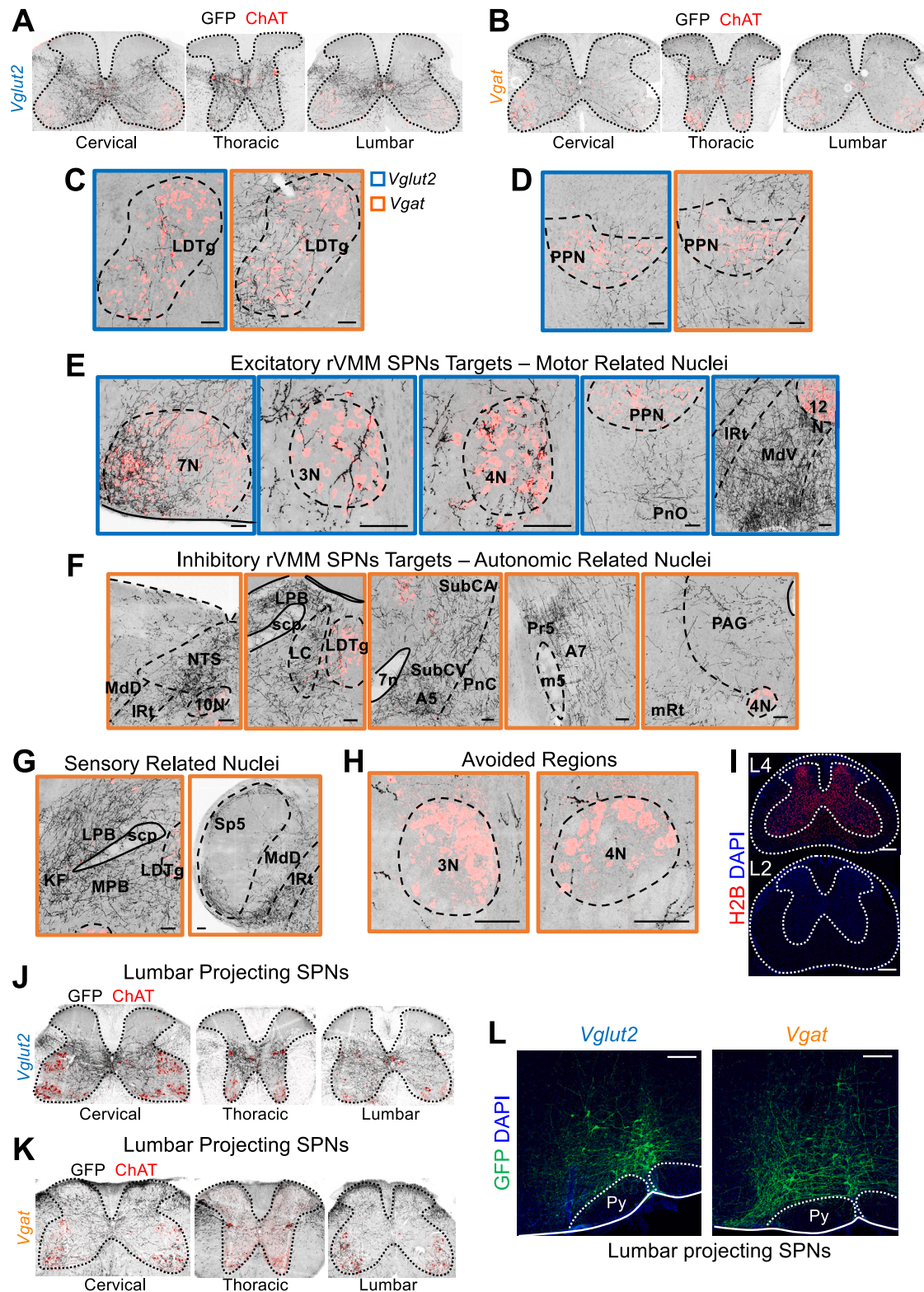
Figure S3. Anatomical innervations of rVMM SPNs in spinal cord and brain regions, related to Figure 4

(A and B) Low-magnitude view of innervation patterns of excitatory (A) or inhibitory (B) rVMM SPNs in different levels of spinal cord co-stained with anti-ChAT antibodies (for all images in this figure).

(legend continued on next page)

(C and D) Innervations of excitatory (blue outline) or inhibitory (orange outline) rVMM SPNs in LDTg and PPN in pons. Synaptophysin-RFP signals are colocalized with axons in the nuclei and not overlaid due to poor visualization. Same results for all images in this figure.

(E) Innervations of excitatory rVMM SPNs in different motor-related nuclei (images with blue outline).

(F and G) Innervations of inhibitory rVMM SPNs in different nuclei related to autonomic and sensory functions.

(H) Inhibitory rVMM SPNs avoid innervation in 3N and 4N.

Scale bar: 100 μm. 12N, hypoglossal nucleus; 10N, dorsal motor nucleus of vagus; IRt, intermediate reticular nucleus; scp, superior cerebellar peduncle; 7n, facial nerve; m5, motor root of the trigeminal nerve. LPB, lateral parabrachial nucleus; MPB, medial parabrachial nucleus; KF, Klliker-Fuse nucleus.

(I) AAV local diffusion indicated by co-injection of AAV9-CAG-H2B-tdTomato in L4/5 spinal cord. Scale bar: 200 μm.

(J and K) Low-magnitude view of spinal innervation patterns of excitatory (J) or inhibitory (K) rVMM SPNs labeled from lumbar spinal cord.

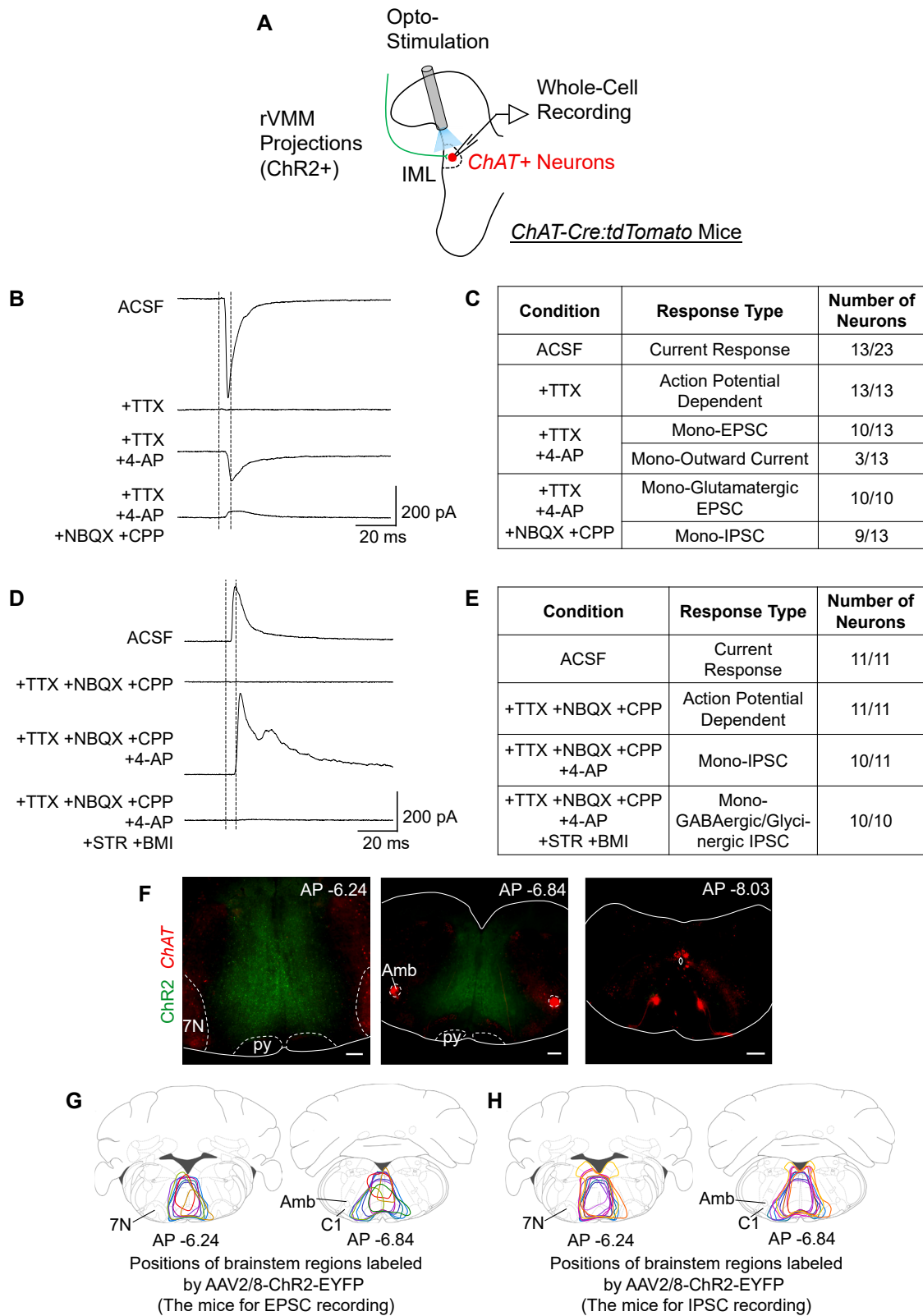(L) Representative images of rVMM SPNs labeled from L4/5. Scale bar: 200 μm.

A

Opto-Stimulation

rVMM Projections (ChR2+)

Whole-Cell Recording

IML

ChAT+ Neurons

ChAT-Cre:tdTomato Mice

B

ACSF

+TTX

+TTX +4-AP

+TTX +4-AP +NBQX +CPP

200 pA

20 ms

C

Condition	Response Type	Number of Neurons
ACSF	Current Response	13/23
+TTX	Action Potential Dependent	13/13
+TTX +4-AP	Mono-EPSC	10/13
	Mono-Outward Current	3/13
+TTX +4-AP +NBQX +CPP	Mono-Glutamatergic EPSC	10/10
	Mono-IPSC	9/13

D

ACSF

+TTX +NBQX +CPP

+TTX +NBQX +CPP +4-AP

+TTX +NBQX +CPP +4-AP +STR +BMI

200 pA

20 ms

E

Condition	Response Type	Number of Neurons
ACSF	Current Response	11/11
+TTX +NBQX +CPP	Action Potential Dependent	11/11
+TTX +NBQX +CPP +4-AP	Mono-IPSC	10/11
+TTX +NBQX +CPP +4-AP +STR +BMI	Mono-GABAergic/Glycinergic IPSC	10/10

F

ChR2 *ChAT*

AP -6.24

7N

py

AP -6.84

Amb

py

AP -8.03

G

7N

AP -6.24

Amb

C1

AP -6.84

Positions of brainstem regions labeled by AAV2/8-ChR2-EYFP (The mice for EPSC recording)

H

7N

AP -6.24

Amb

C1

AP -6.84

Positions of brainstem regions labeled by AAV2/8-ChR2-EYFP (The mice for IPSC recording)

(legend on next page)

Figure S4. Synaptic connections between rVMM SPNs and sympathetic preganglionic neurons, related to Figure 4

(A) Scheme showing recording from tdTomato^{+} cells in the thoracic spinal cord slices of *ChAT-Cre: tdTomato* mice.

(B) An example of current response to optic stimulation in four conditions: ACSF; +TTX; +TTX and 4-AP; and +TTX, 4-AP, and NBQX/CPP. Dotted vertical lines indicating the light stimulation period (5 ms).

(C) Summary table of response types from total 23 neurons recorded.

(D) An example of mono-synaptic IPSC isolation and its senstivity to glycine and GABA$_A$ receptor antagonists. Mono-synaptic IPSC was isolated in the condition of TTX + NBQX + CPP + 4-AP and blocked by the addition of strychnine and bicuculine.

(E) Summary table of response types from 11 neurons recorded.

(F) Representative images showing ChR2 expression in rVMM in coronal sections. Scale bar, 200 μm.

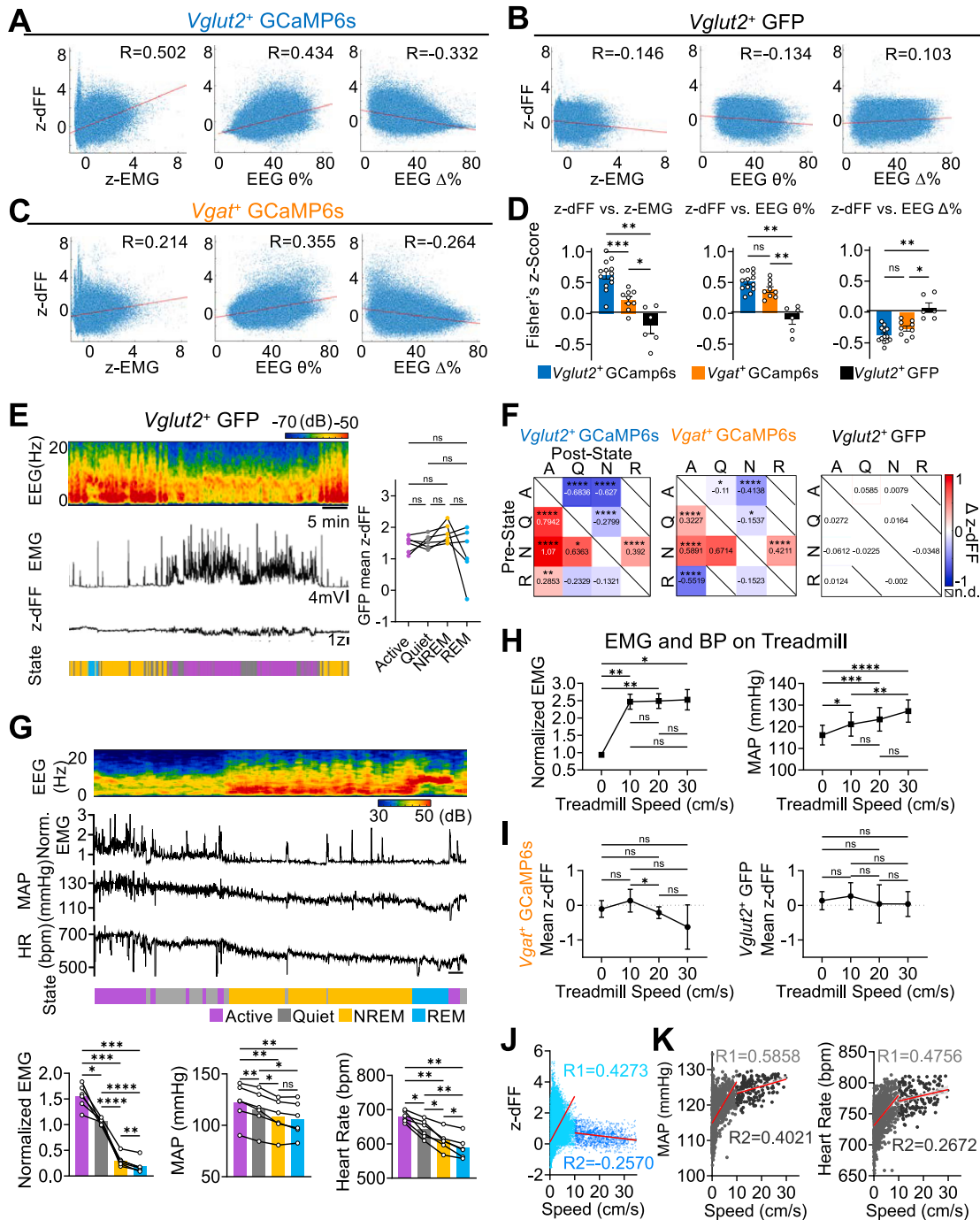(G and H) Outlines of ChR2-EYFP expression area in the brainstem for EPSC (G) and IPSC (H) experiments (14 mice).

Figure S5. EMG, sympathetic activities, and the activities of rVMM SPNs at different arousal states, related to Figure 5

(A) Pearson correlation analysis of *Vglut2⁺* rVMM SPNs calcium activity and neck *Z* scored EMG, EEG theta-band power density, and delta-band power density. Correlation coefficient (CC), R, and the fit line (red) were superimposed. Data were combined from 9 animals, 13 recordings. All *p* values < 0.0001.

(B) Pearson correlation analysis of GFP signal of *Vglut2⁺* rVMM SPNs and neck z-EMG, EEG theta-band power density, and delta-band power density. Correlation coefficient (CC), R, and the fit line (red) were superimposed. Data were combined from 6 animals. All *p* values < 0.0001.

(C) Pearson correlation analysis of *Vgat⁺* rVMM SPNs calcium activity and neck z- EMG, EEG theta-band power density, and delta-band power density. Correlation coefficient (CC), R, and the fit line (red) were superimposed. Data were combined from 7 animals, 9 recordings. All *p* values < 0.0001.

(D) Comparison of CC between each group of mice (CC was converted to Fisher *Z* score). Left, comparison between CC of z-dFF and z-EMG; Middle, comparison between CC of z-dFF and EEG theta-band power; Right, comparison between CC of z-dFF and EEG delta-band power; data were presented as mean ± SEM;

$n = 13$ for *Vglut2*^{+} Gcamp6, $n = 9$ for *Vgat*[+] Gcamp6, and $N = 6$ for *Vglut2*^{+} GFP. ****, $p < 0.0001$; ***, $p < 0.001$; **, $p < 0.01$; ns, not significant. One-way ANOVA with Fisher's LSD multiple comparisons test.

(E) Recording example and analysis of GFP signal from *Vglut2*^{+} rVMM SPNs. Left: 1 h recording of EEG, Z scored EMG, and Z scored dFF. Corresponding mouse states were indicated at the bottom. Right: group comparison of GFP signals from *Vglut2*^{+} rVMM SPNs between different states (mean, $n = 5$). ns, not significant. One-way ANOVA with Fisher's LSD multiple comparisons test.

(F) Heatmap showing z-dFF changes during state transitions (post-state mean z-dFF minus pre-state mean z-dFF). *, $p < 0.05$; **, $p < 0.01$; ****, $p < 0.001$; n.d., not determined. Paired t test. A, active; Q, quiet; N, NREM; R, REM.

(G) Upper: representative traces of the EEG power spectrum, EMG amplitude, MAP, and HR at different arousal states. Scale bar, 60s. Lower: mean and individual values of EMG amplitude, MAP, and heart rate at different arousal states. *, $p < 0.05$; **, $p < 0.01$; ***, $p < 0.001$; ****, $p < 0.0001$; ns, not significant; repeat-measures one-way ANOVA with Tukey's multiple comparisons test.

(H) Average ($\pm$SEM) of EMG peak amplitudes and blood pressure levels at different treadmill running speeds (mean $\pm$ SEM, $n = 10$). *, $p < 0.05$; **, $p < 0.01$; ***, $p < 0.001$; ****, $p < 0.0001$; ns, not significant. Repeat-measures one-way ANOVA with Tukey's multiple comparisons test.

(I) Left: mean Z scored dFF of GCaMP6s in *Vgat*[+] rVMM SPNs at four different speeds (mean $\pm$ SEM, $N = 7$). Right: mean Z scored dFF of GFP in *Vglut2*^{+} rVMM at four different speeds (mean $\pm$ SEM, $N = 6$). *, $p < 0.05$; ns, not significant; mixed-effects analysis with Fisher's LSD multiple comparisons test.

(J) Pearson correlation analysis of z-dFF and speed on a disc and linear fitting curve (red) with 95% confidence bands (gray). A threshold of 10 cm/s was used to separate the data into two groups for correlation analysis. R1 and R2, Pearson correlation coefficients for the speed of 0 to 10 cm/s and >10 cm/s, respectively.

(K) Pearson correlation analysis and linear fitting curve (red) with 95% confidence bands (gray shade). Data points were collected from traces (on a disc) smoothed with 1-s window and down-sampled to 0.2 Hz. R1 and R2, Pearson correlation coefficients for the speed of 0 to 10 cm/s and >10 cm/s, respectively.
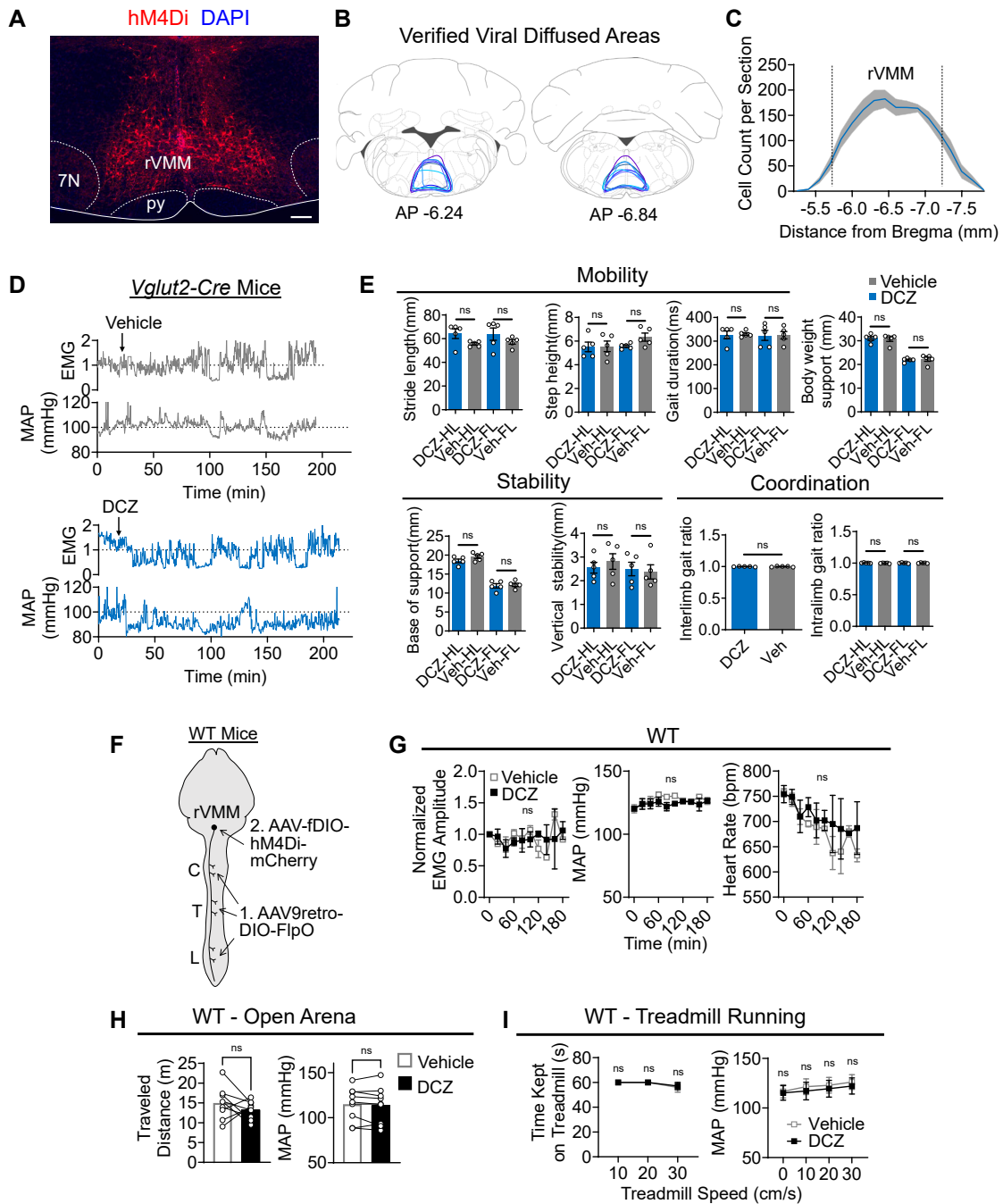
Figure S6. Characterization of DCZ-mediated silencing of excitatory rVMM SPNs, related to Figure 6

(A) Representative coronal brain section of hM4Di-mCherry expression in *Vglut2*^{+} SPNs in rVMM. Scale bars, 200 μm.

(B) Diffusion areas of hM4Di expression at two coronal levels of rVMM. Subjects are individually colored (*n* = 7).

(C) Rostral-caudal distribution of hM4Di expressing cells (mean ± SEM, *n* = 7). The rostral and caudal boundaries of rVMM are marked by dot line.

(D) Representative EMG and MAP traces upon vehicle or DCZ treatment of Vglut2-Cre mice with hM4Di expression.

(E) Kinematic parameters of forelimb (FL) and hindlimb (HL) from ground locomotion of *Vglut2-Cre* mice with hM4Di expression, mean ± SEM, *n* = 5. ns, not significant; paired t test.

(F) Strategy of injecting same viruses in WT mice as control group.

(legend continued on next page)

(G) Time course of EMG, MAP, and heart rate (mean ± SEM) upon vehicle or DCZ treatment in control group ($n = 3$). ns, not significant; mixed-effects analysis with Bonferroni's multiple comparisons test.

(H) Performance of WT control group in open arena (mean and individual value) upon vehicle or DCZ treatment ($n = 9$). ns, not significant; paired t test.

(I) Performance of WT control group in treadmill running upon vehicle or DCZ treatment ($n = 9$). ns, not significant; two-way ANOVA with Tukey's multiple comparisons test.
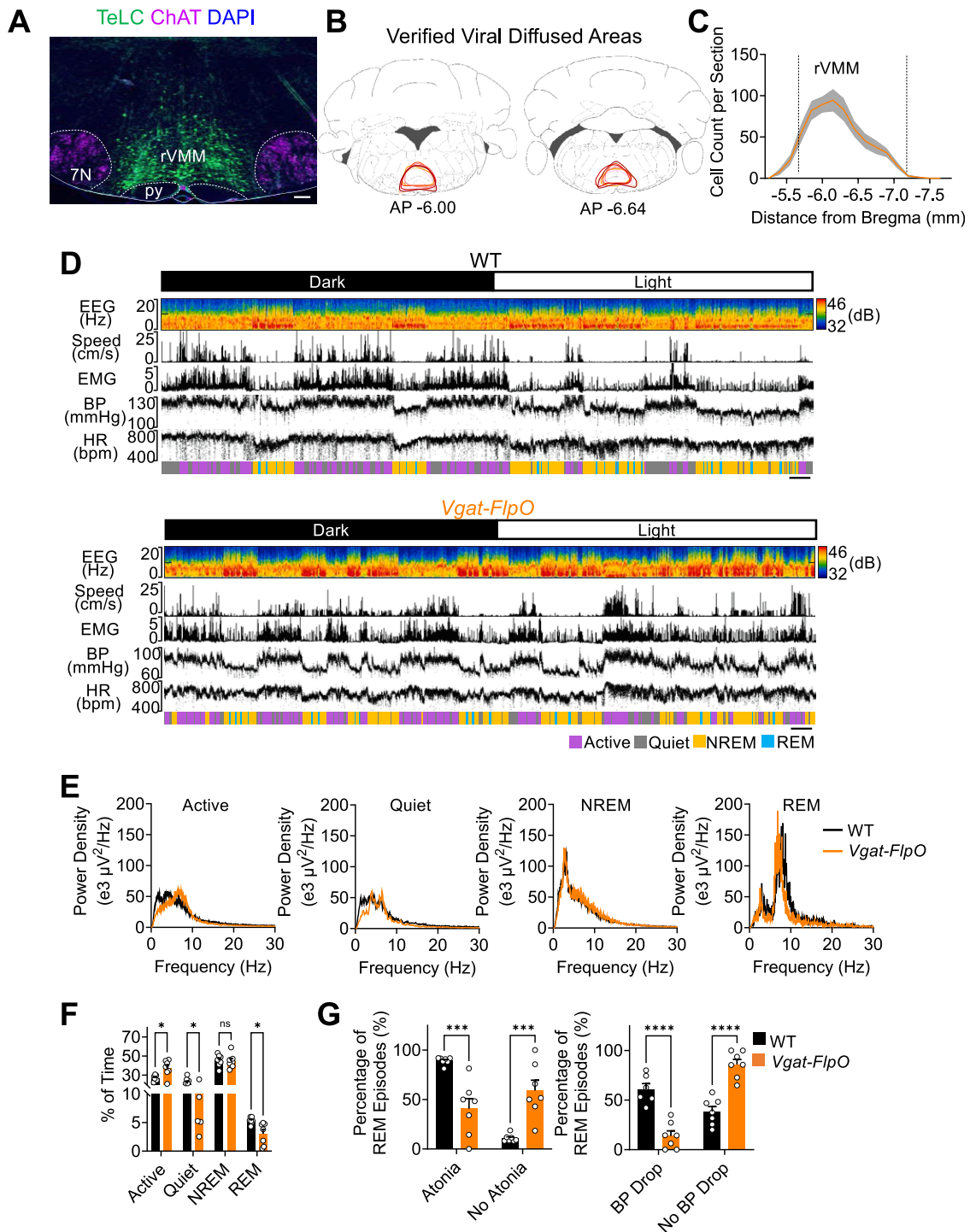
Figure S7. Characterization of TeLC-mediated silencing of inhibitory rVMM SPNs, related to Figure 7

(A) Representative coronal brain section of TeLC-EYFP expression in *Vgat*[+] SPNs in rVMM. Scale bars, 200 μm.

(B) Diffusion areas of TeLC expression at two coronal levels of rVMM. Subjects are individually colored (*n* = 7).

(C) Rostral-caudal distribution of TeLC expressing cells (mean ± SEM, *n* = 7). The rostral and caudal boundaries of rVMM are marked by dotted lines.

(D) Representative traces of EEG power spectrum, body mass speed, EMG amplitude, blood pressure, and heart rate in dark-light cycle of WT and *Vgat-FlpO* mice. Scale bars, 30 min.

(E) EEG power spectrum of the four arousal states of representative WT and *Vgat-FlpO* mice.

(F) Average percentage (±SEM) of time spent in different behavioral states. *, $p < 0.05$; ns, not significant; unpaired t test.

(G) Average percentage (±SEM) of REM sleep episodes with or without atonia/BP drop. ***, $p < 0.001$; ****, $p < 0.0001$; two-way ANOVA with Bonferroni's multiple comparisons test.